J. Fluid Mech. (1995), *vol.* 302, *pp.* 333–376

Direct numerical simulation of turbulent flow over a modelled riblet covered surface

By D. GOLDSTEIN[1]†, R. HANDLER[2] AND L. SIROVICH[1]

[1]Center for Fluid Mechanics, Brown University, Providence, RI 02912, USA

[2]Naval Research Laboratory, Washington, DC 20375, USA

(Received 23 August 1992 and in revised form 25 April 1995)

An immersed boundary technique is used to model a riblet covered surface on one wall of a channel bounding fully developed turbulent flow. The conjecture that the beneficial drag reduction effect of riblets is a result of the damping of cross-flow velocity fluctuations is then examined. This possibility has been discussed by others but is unverified. The damping effect is explicitly modelled by applying a cross-flow damping force field in elongated streamwise zones with a height and spacing corresponding to the riblet crests. The same trends are observed in the turbulence profiles above both riblet and damped surfaces, thus supporting cross-flow damping as a beneficial mechanism. It is found in the examples presented that the effect of the riblets on the mean flow field quantities (mean velocity profile, velocity fluctuations, Reynolds shear stress, and low-speed streak spacing) is small. The riblets cause a relatively small drag reduction of about 4%, a figure that is in rough agreement with experiments and other computations. The simulations also suggest a mechanism for the observed displacement of the turbulence quantities away from the wall.

The immersed boundary technique used to model the riblets consists of creating an externally imposed spatially localized body force which opposes the flow velocity and creates a riblet-like surface. For unsteady viscous flow the calculation of the force is done with a feedback scheme in which the velocity is used to iteratively determine the desired value. In particular, the surface body force is determined by the relation $\boldsymbol{f}(\boldsymbol{x}_s, t) = \alpha \int_0^t \boldsymbol{U}(\boldsymbol{x}_s, t')\mathrm{d}t' + \beta \boldsymbol{U}(\boldsymbol{x}_s, t)$ for surface points $\boldsymbol{x}_s$, velocity $\boldsymbol{U}$, time t and negative constants α and β. All simulations are done with a spectral code in a single computational domain without any mapping of the mesh. The combination of the immersed boundary and spectral techniques can potentially be used to solve other problems having complex geometry and flow physics.

1. Introduction

It has been found experimentally that surfaces possessing streamwise grooves (riblets) are capable of reducing turbulent flow skin friction. Walsh (1990) and Coustols & Savill (1992) provide comprehensive reviews of the experimental work on the riblet drag reduction effect. Related concepts date back to a German patent application (Kramer 1937) which suggested that suspended streamwise wires could shield the wall region from outer-region turbulent fluctuations. The incentive for finding a general purpose and easily manufactured passive surface texture which

† Present address: Department of Aerospace Engineering and Engineering Mechanics The University of Texas at Austin, Austin, TX 78712, USA.

reduces skin friction drag is clear. Effective textures have generally been found to be ridges having triangular, cusped, or rectangular cross sections and, in fact, a plastic film having sub-millimetre scale triangular riblets which may be applied to a surface has been developed commercially.

The idea for riblets appears to have come from three sources. Kennedy, Hsu & Liu (1973) suggested that the shear stress in corners would be reduced based on the observation that the wall shear is reduced in the corners in square duct turbulent flow. Liu, Kline & Johnston (1966) thought that long fences could be used to confine the growth of the streamwise boundary layer vortices. These vortices are thought to be responsible for the up-welling of low-speed fluid away from the wall thus causing low-speed boundary layer streaks. Liu *et al.* wished to arrest the formation and ejection of larger scale eddies away from the wall as well as to suppress the finer scale turbulence. Finally, Bechert, Hoppe & Reif (1985), Bechert *et al.* (1986), Bechert (1987), Bechert & Bartenwerfer (1989) and Bechert, Bartenwerfer & Hoppe (1990) and Bruse *et al.* (1993) suggested an analogy with the ridges found on the scales of fast swimming sharks.

Experimental drag reduction obtained from riblet surfaces has been disappointing–generally less than 10%. The underlying ideas motivating the use of ribbed surfaces may be flawed. While drag in the corners or valleys of the ribs is reduced, drag on the peaks is increased so that in a laminar flow the drag on the ribbed surface is greater than that over a smooth surface (Choi, Moin & Kim 1991*a*). In fact, Kennedy *et al.*'s (1973) results showed a drag increase in turbulent flow as well. Regarding the explanation of Liu *et al*, if riblets are spaced widely enough to surround a boundary layer vortex, they produce a substantial drag increase rather than a decrease. Finally, tests with shark skin itself have been ambiguous; dried or even fresh skin may not be representative of the effects on living sharks. The experimental shark skin model tested by Bruse *et al.* showed only a small drag reduction. Other fast-swimming creatures do not have ribbed skin, so shark scale ribs may serve purposes other than drag reduction.

While riblets decrease drag in some cases they increase it in others. A riblet covered surface has appreciably greater wetted surface area than a flat surface. The riblet peaks project into the high-speed near-wall flow and suffer much greater shear stress than do the valleys where the flow is slow. The riblets also alter the mean flow above the wall and the one- and two-point turbulence correlation quantities. Somehow, these various effects act in concert to produce the net drag reductions observed experimentally. A satisfactory explanation of the physical mechanisms which cause net drag reduction remains elusive.

Recently it has become feasible to consider direct numerical simulation of turbulent flow over a riblet covered surface. Earlier computational efforts of Khan (1986) and Djenidi, Squire & Savill (1991) used turbulence models whose applicability might be questionable, e.g., the particular assumption of local isotropy of small-scale flow structures close to the riblets. The present work focuses on turbulent flow over riblets by directly integrating the equations of motion. Others have begun such simulations as well: Choi *et al.* (1991*a*) used a finite difference approach to simulate steady laminar flow over riblets and found that the drag increase became more pronounced as the ribs projected further into a channel flow. Choi *et al.* (1991*b*) have also extended their calculations to turbulent flow and found drag decreases in agreement with experiments. Chu, Henderson & Karniadakis (1992) and Chu & Karniadakis (1993) have used the spectral element-Fourier approach to study laminar, transitional, and turbulent flow over ten triangular riblets in a narrow channel and find drag reductions. Currently full direct numerical simulations are expensive because of the

range of flow scales which must be represented and because drag effects are small and require long time integrations.

The present work uses a different computational approach. In the spectral code used here, riblets are modelled by applying a body force to the flow near one of the channel walls so as to bring the flow to rest on a riblet shaped virtual surface. This approach for creating a virtual solid surface, has been shown (Goldstein, Handler & Sirovich 1993*a*) to be sufficient to model laminar and turbulent flow over complicated geometries. That work also provides a discussion of the numerical stability of the method. A review of the virtual surface approach (also referred to as the immersed boundary method) will now be given.

When fluid flows over a body, it exerts a normal (pressure) force on the surface and also exerts a shear force. Conversely, the surface exerts a force of opposite sign on the fluid; in the no-slip case, this localized force is what brings the fluid to rest on the body. The fluid 'sees' a body through the forces of pressure and shear that exist along the surface. In an unsteady flow, such surface forces vary in time. Equivalently, if one applies the appropriate set of forces to the fluid, it will flow as if it were passing over a solid object. That is, the effect of certain boundary conditions can be mimicked with an equivalent external force field rather than with a specification of boundary conditions. Thus, flow about an arbitrary body can be computed in a simple computational domain with the body replaced by a force field.

Immersed boundary techniques have been applied extensively to model moving boundaries: heart valves (Peskin 1972; Peskin & McQueen 1980), a beating heart (Peskin 1977; Peskin & McQueen 1989; McQueen & Peskin 1980), a swimming fish-like structure (Fauci & Peskin 1988), and flexible particles in suspension (Fogelson & Peskin 1988). The basis of these models is that the solid being modelled is defined by a set of connected boundary points which move (in the Lagrangian sense) through a fixed (Eulerian) mesh. The boundary points are connected by elastic links which create internal forces (to the body) that are transmitted to the surrounding fluid since the boundary points and the links are massless. The interior particle forces, calculated by an approximately implicit scheme or an implicit scheme (Tu & Peskin 1992) provide part of the force density in the Stokes or Navier–Stokes equations. The forces and velocities are interpolated between the boundary points and the fixed mesh. Sulsky & Brackbill (1991) modelled elastic particles in a suspension where the force density in the particles is related to the displacement field computed from the stress–strain constitutive equations for an elastic solid. The flow is computed with a finite volume technique; interior as well as surface points represent the solid body. Unverdi & Tryggvason (1992) modelled droplets using a localized body force to simulate the effects of surface tension. They used front-tracking particles to maintain the separation between two fluids and calculated the entire flow with a finite difference approach.

The works cited above were primarily concerned with boundaries moving through a fixed mesh and the flow field was computed with a finite difference/volume element approach. The boundaries move with the local flow velocity. The forces between boundary points, rather than the relative (or absolute) location of the boundary points, are what is specified in these schemes. In these approaches the force computation is fairly complex as it must model the interior stresses and strains of the solid. If the locations of the boundary points (rather than the forces between them) are specified, the problem is simpler. The force produced by each point may then be computed independently (Peskin 1972; Fauci 1991). In Fauci (1991) this approach has been combined with a vortex blob technique and has been shown to provide qualitatively

accurate solutions. An earlier related approach is that of Viecelli (1969, 1971) in which a shear-free surface is modelled with an adaptive pressure field in a marker and cell technique. The pressure along some desired boundary is used to enforce the no-through-flow condition; if fluid flows through the boundary the pressure is increased on the boundary until the through-flow ceases.

In the work to be presented here, and in contrast to the work cited above, the range of applicability of the immersed boundary technique has been extended to fully turbulent flows on a fixed grid in a fully spectral code. A key feature of the present approach is that flows in complex geometries are reduced to ones which are rectilinear and hence are amenable to spectral methods. Reduction to spectral codes is achievable in other ways, most notably by the mapping of a complex domain to one that is rectilinear. Our method may be put into perspective by contrasting it with what can be expected from a such mapping. A mapping procedure generally leads to Poisson and other operators with non-constant coefficients. These can be efficiently solved by iterative methods (Orszag 1980). In general, however, the iterative solutions impose significant computational overhead, not to mention a substantial additional coding effort. By comparison, the virtual surface approach imposes only a small computational overhead, roughly 5% more computational time per time step in the calculations presented here, and little in the way of a coding burden. The memory overhead is small and scales with the number of surface grid points. We also have found that numerical stability is only modestly affected by the introduction of virtual textured surfaces in our codes. Finally, although we do not treat such issues here, the approach can easily be adapted to cases in which moving boundaries are present (see Goldstein, Adachi & Isumi 1993*b*, Saiki & Biringen 1995 and the works related to Peskin's approach mentioned above).

2. Virtual surface approach

The incompressible Navier–Stokes equations with an external force field are written as follows:

$$\frac{\partial \boldsymbol{U}}{\partial t} = \boldsymbol{U} \times \boldsymbol{\Omega} - \boldsymbol{\nabla}\left(p/\rho + \frac{\boldsymbol{U}\cdot\boldsymbol{U}}{2}\right) + \nu\nabla^2\boldsymbol{U} + \boldsymbol{f} \tag{1a}$$

and

$$\boldsymbol{\nabla}\cdot\boldsymbol{U} = 0. \tag{1b}$$

Here, t is time, $\boldsymbol{U} = (U, V, W)$ is the velocity in rectangular coordinates (x, y, z), $\boldsymbol{\Omega}$ is the vorticity, p is the pressure, ρ is the density, and ν is the kinematic viscosity. The force $\boldsymbol{f}$ in (1*a*), which is used to generate a virtual surface, is given by

$$\boldsymbol{f}(\boldsymbol{x}, t; \boldsymbol{x}_s) = \boldsymbol{g}(\boldsymbol{x}, t)\delta(\boldsymbol{x} - \boldsymbol{x}_s) \tag{2}$$

where the position vector $\boldsymbol{x}_s$ locates the bounding surface and $\boldsymbol{g}(\boldsymbol{x}, t)$ is a feedback forcing which will be given below. A more detailed presentation of this formalism, given by Salathe & Sirovich (1967) and Sirovich (1967, 1968), justifies and demonstrates several aspects of the formalism developed in Goldstein *et al.* (1993*a*).

The object of the virtual surface approach is to determine $\boldsymbol{g}(\boldsymbol{x}, t)$ such that the fluid motion is brought to rest (for a no-slip boundary) at $\boldsymbol{x}_s$. To accomplish this the force

is made to adapt itself to the local flow field.† In particular, consider a force field given by

$$\boldsymbol{g}(\boldsymbol{x},t) = \alpha \int_0^t \boldsymbol{U}(\boldsymbol{x},t')\mathrm{d}t' + \beta \boldsymbol{U}(\boldsymbol{x},t) \tag{3}$$

where the quantities α and β are chosen to be negative constants (see Goldstein *et al.* 1993*a*). This force field represents an explicit feedback of the time integral of the velocity and the velocity itself. One might at first think that using concepts from linear control theory in simulations of turbulent and highly nonlinear flows would be difficult, especially because the control is digital rather than analog (Dorf 1983). Yet, as will be seen, one needs only to control small regions of the flow where near-linear responses are expected. The first term in (3) with integral feedback is alone sufficient to create a force field that will bring the flow to rest on the surface points. For example, if $\boldsymbol{U}$ is greater than zero, the force will increase with time in a direction opposite to that of $\boldsymbol{U}$ until the flow comes to rest. This is the restorative or spring force. The second term can be thought of as representing a force created by the Stokes drag of an obstacle that is too small to be resolved. This force applies damping and might, for example, represent the drag on a fine hair located at $\boldsymbol{x}$.

This simple feedback on boundary points may be thought of as creating a force field that 'learns' to simulate the desired boundary condition. In an unsteady flow, the gain α must be large enough so that the resulting response time of the forcing (natural frequency $= (1/2\pi)|\alpha|^{1/2}$) is faster than the most energetic flow frequencies in order that the force field can track the changing flow. The method by which the time integral is evaluated will determine the maximum magnitude of α to ensure stability. In the simulations discussed below, the time integral is approximated simply by a Riemann sum:

$$\int_0^t \boldsymbol{U}(\boldsymbol{x},t')\mathrm{d}t' \approx \sum_{j=1}^{N} \boldsymbol{U}(\boldsymbol{x},j)\Delta t \tag{4}$$

where N is the number of steps, and Δt is the size of the time step. The time marching of the forcing term is done with a second order accurate Adams–Bashforth scheme. We find that the stability limit for the time step is approximately given by

$$\Delta t < \frac{\beta + (\beta^2 - 2\alpha k)^{1/2}}{\alpha} \tag{5}$$

where k is a problem-dependent constant of order one. With moderate integral gain the viscous forces and the $\beta \boldsymbol{U}$ term damp out the spring/mass-type temporal oscillations. It should be noted that the force $\boldsymbol{f}$ depends only on the flow at $\boldsymbol{x}_s$ and that the forces at different boundary points do not interact except through the mediation of the fluid. The computational time for each virtual surface location is small (simply updating (4) and evaluating (3)) so that the total additional time for utilizing a virtual surface is simply proportional to the number of boundary points. It is not necessary to bring the flow to rest within the body. In fact, as will be seen shortly, fluid will in general flow below the modelled riblet surface (inside the solid) while the velocity is forced to be zero on the riblet surface itself.

† The force field $\boldsymbol{f}$ can be determined in a number of different ways but the the force required is unique in that there can be only one force which creates the no-slip and no-through-flow condition. Conversely, at some instant in time the flow would create only one pattern of surface forces.

3. Numerical methods

3.1. *Description of the spectral code*

A spectral method code (Kim, Moin & Moser 1987; Handler, Hendricks & Leighton 1989) is used to solve the governing incompressible Navier–Stokes equations. We consider a channel, periodic in the streamwise (x) and spanwise directions (z) and bounded by impermeable flat surfaces in the vertical direction (y). Flow quantities are represented by Fourier expansions in the horizontal (x,z)-plane and a Chebyshev expansion in the wall normal direction. It is convenient, because of the numerical method used, to add the force $\boldsymbol{f}$ to the nonlinear term $\boldsymbol{U} \times \boldsymbol{\Omega}$ since both terms are most efficiently evaluated in physical space. De-aliasing in the x- and z-directions occurs during the plane by plane evaluation of $\boldsymbol{U} \times \boldsymbol{\Omega}$ by interpolating $\boldsymbol{U}$ and $\boldsymbol{\Omega}$ onto a grid having 3/2 as many collocation points in each direction. The force field required is then also calculated on this expanded grid. Because these collocation points may not correspond to the regular grid sites, the surfaces created with the force field are properly interpreted only on the expanded grid.

In order to generate a smooth surface rather than a step-like surface the force field given by (2) is modified in the two periodic directions by using a narrow Gaussian distribution as follows:

$$\boldsymbol{f}(\boldsymbol{x},t) = \sum_{\text{all } \boldsymbol{x}_s} \boldsymbol{f}(\boldsymbol{x}_s,t) \mathrm{e}^{-\epsilon[(i-i_s)^2+(k-k_s)^2]} \tag{6}$$

where the surface point $\boldsymbol{x}_s$ is located at grid site (i_s, j_s, k_s) and point $\boldsymbol{x}$ is located at grid site (i,j,k). With $\epsilon = 1$ the immediately adjacent points receive about 37% of the central force while points two grid sites further away receive essentially none. The effect of this local smoothing is to blur the exact location of the surface and extend its reach slightly. Hence, the exact location of the surface is blurred over about one grid site. If sufficient spatial resolution has been used one finds that the exact smoothing function is not critical provided it has similar compact support. In the simulations of three-dimensional flow discussed below, such spatial smoothing is not done in the Chebyshev direction.

Introducing nearly point forces into a spectral representation of the flow poses some unique problems since singularities tend to produce spatial oscillations that, if left alone, simply remain at about constant amplitude during the calculation. As might be expected, the oscillations were by far the greatest at the highest wavenumbers and were insignificant at lower wavenumbers.

It was found that two relatively benign remedies could effectively remove these oscillations. In the Chebyshev direction as well as in the Fourier directions, mild spectral smoothing is used. The spectral coefficients of the quantity $\boldsymbol{U} \times \boldsymbol{\Omega} + \boldsymbol{f}$ are multiplied at every time step by a low pass filter function, K, given by:

$$K = \mathrm{e}^{\xi_2(n_x/N_x)^{\xi_1}} \mathrm{e}^{\xi_2(n_y/N_y)^{\xi_1}} \mathrm{e}^{\xi_2(n_z/N_z)^{\xi_1}} \tag{7}$$

where (n_x, n_y, n_z) are the spectral mode indices in the (x,y,z)-directions and (N_x, N_y, N_z) are the total number of modes in those directions. The decay constant $\xi_1 = 20$ is chosen so there will be a sharp cutoff of the highest modes and $\xi_2 = -1$ is used so the highest wavenumber will be reduced by a factor of 1/e. These values of ξ_1 and ξ_2 produce a filter K with the first 86% of the modes of $\boldsymbol{U} \times \boldsymbol{\Omega} + \boldsymbol{f}$ having over 95% of their original energy at each step. The exact values of the constants should not be important as long as the natural energy cascade has generated little energy at the highest wavenumbers. Similar spectral smoothing has been employed by others

as well (Gottlieb, Hussaini & Orszag 1984). Of course, with greater resolution this smoothing will have less influence on the flow because there will naturally be less energy in the highest modes. It does not appear necessary to remove the highest modes more completely.

A second smoothing method is to create a flow inside the virtual solid body (below the riblets) to reduce kinks that otherwise develop in the mean velocity profile. The idea is analogous to potential flows past bodies for which an internal flow, usually not of interest, is created in the course of solving the problem. In the present instance, the force field maintains the no-slip condition on riblet surfaces. Internal flows below the riblet virtual surface are created simply for numerical reasons to provide a globally smooth velocity field. See Goldstein *et al.* (1993*a*) for a more detailed description of the internal flows used.

3.2. *Tests of the virtual surface approach*

The effect of interest, drag reduction by the riblets, is expected to be small (0 to 10%). Such drag reduction is a result of the balance between the alteration of the dynamics of the near wall turbulence and the increased wetted surface area presented by the corrugated surface. The determination of surface drag due to turbulent flow over riblets requires long time averaging to obtain a satisfactorily low sampling error. It is not feasible to perform a significant sweep of the possible sources of error (grid resolution, smoothing techniques, etc.) for a fully turbulent flow. Instead, two related but simpler problems whose solutions are better understood are examined: laminar steady flow over riblets and fully turbulent flow over a flat plate. Laminar flow over riblets has been simulated by Choi *et al.* (1991*a*), Chu *et al.* (1992) and Chu & Karniadakis (1993) while turbulent flat wall channel flow has been studied numerically and experimentally by many others (see Kim *et al.* 1987 and Handler *et al.* 1989 and the references therein.) The case of laminar flow over riblets will illustrate the sensitivity of the present solution procedure to varying grid resolution, different smoothing techniques, and the boundary conditions imposed below the riblets. The turbulent flat-plate simulations will demonstrate that the time accuracy of the force field approach is sufficient for the simulation of turbulent flow over riblets.

3.2.1. *Laminar flow over riblets*

A number of simulations of laminar flow over riblets were performed using the virtual surface approach. A summary of the computational parameters used in each of these simulations is given in tables 1–3. Simulations tabulated in table 1 (runs 1–16) were used to demonstrate the effects of grid resolution on five different riblet geometries. The effects of different smoothing techniques are studied in the simulations summarized in table 2. Runs 17–20 illustrate the effects of spectral smoothing (ξ_1 and ξ_2 varied), runs 21–24 illustrate the effects of a different internal force field below the rib (G_{rev}, a pressure gradient force of opposite sign to the pressure gradient driving the bulk of the flow, G, is varied), and runs 25–27 illustrate the effects of spatial smoothing of the force field (ϵ varied). Runs 28–31 (table 3) illustrate the effects of the boundary conditions applied below the riblet surface.

Although the laminar flows considered here are two-dimensional, varying only in y and z with a mean flow in the x-direction, a fully three-dimensional code was used ($N_x = 4$) since a strictly two-dimensional code was not available. In these simulations a single riblet is created by applying the force field (see (3)) along a sequence of grid sites near the lower channel boundary as seen in figure 1. These points lie on the expanded 3/2 grid which has a cosine grid spacing in the y-direction

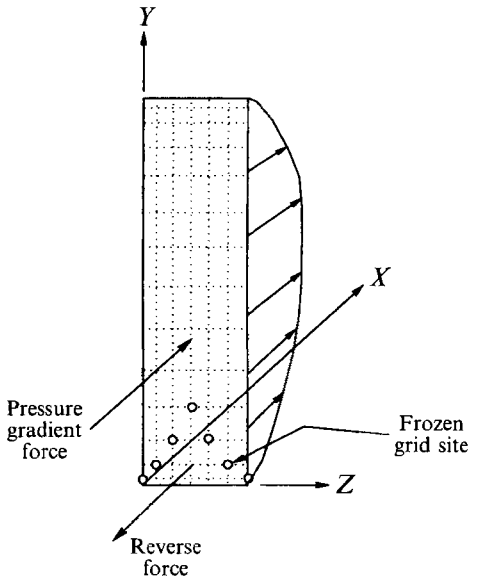

FIGURE 1. Geometry for laminar flow simulation of channel bounded by two impermeable boundaries and containing a single virtual riblet surface. A uniform pressure gradient is applied above the riblet and a pressure gradient of opposite sign is applied below.

($y_j = \cos[\pi(j-1)/N_y]$, $j = 1, 2, 3 \ldots N_y$). If the frozen (forced) sites are spaced evenly in z and incremented and decremented in y (e.g. for a rib made of seven grid points, $(j_s, k_s) = (2,1), (3,2), (4,3), (5,4), (4,5), (3,6)$ and $(2,7)$) the riblets have a cusped shape due to the cosine grid.

The initial condition for these simulations was a laminar (parabolic) profile given by $u/u_{cl} = 1-(y/h)^2$, where h is the channel half-width, u_{cl} is the centreline velocity, and the Reynolds number, $Re_{cl} = u_{cl}h/\nu$, was chosen to be 1000. The driving pressure gradient was constant in time as it is for all simulations to be presented in this work. The equations of motion (1*a,b*) are scaled in such a way that the non-dimensional pressure gradient, G, is given by $G = (R^*/R_{cl})^2$, where $R^* = u^*h/\nu$ is the friction Reynolds number, u^* is the friction velocity given by $u^* = (\tau_w/\rho)^{1/2}$, and τ_w is the shear stress at the wall. In these laminar simulations, R^* was chosen so that the pressure gradient, G, exactly balances the wall shear stress generated by the initial parabolic profile. Here, $R^* = (2R_{cl})^{1/2}$ for plane channel flow so that $R^* = 44.72$ and $G = 2 \times 10^{-3}$.

At time $t = 0$, the riblet surface is generated near one wall of the channel using the virtual surface approach and unsteady laminar flow results in which the drag on both flat and ribbed surfaces varies in time. The simulations were run until a steady-state is achieved, which is defined here as the time at which the ratio of the drag on the riblet side to the drag on the flat side (the drag ratio DR) changes less than 3×10^{-9} per time step. The drag on the ribbed surface can be computed at any time from an instantaneous momentum balance involving the rate of change of momentum, the drag on the flat surface (both of which can be computed exactly at any instant), and the driving pressure gradient.

The effects of spatial resolution (table 1) are now considered. For these simulations a sample of typical riblet geometries is given (figure 2). The rib angle θ is defined as the angle between the Z-axis and the line segment connecting the riblet valley and the crest. Hence, the ratio of rib height to width is $(1/2)\tan(\theta)$. For future reference

Run	N_y	N_z	ϵ	BC	(ξ_1, ξ_2)	AR	θ	(α, β)	G_{rev}	DR
					Geometry for a medium 20° riblet					
1	64	6	2	S	(20,−1)	8.4	20.0	(10,1)	4	1.00875
2	128	12	2	S	(20,−1)	8.4	20.0	(10,1)	4	1.00576
3	256	24	2	S	(20,−1)	8.4	20.0	(10,1)	4	1.00489
					Geometry for a small 44° riblet					
4	32	4	2	S	(20,−1)	12.8	44.0	(10,1)	4	1.0322
5	64	8	2	S	(20,−1)	12.8	44.0	(10,1)	4	1.0256
6	128	16	2	S	(20,−1)	12.8	44.0	(10,1)	4	1.0219
7	256	32	2	S	(20,−1)	12.8	44.0	(10,1)	4	1.0203
					Geometry for a large riblet					
8	32	10	2	S	(20,−1)	3.4	45.0	(10,2)	4	1.1240
9	64	20	2	S	(20,−1)	3.4	45.0	(10,2)	4	1.1064
10	128	40	2	S	(20,−1)	3.4	45.0	(10,2)	4	1.1002
11	256	80	2	S	(20,−1)	3.4	45.0	(10,2)	4	1.0974
					Geometry for a small sharp riblet					
12	64	10	2	NS	(−,0)	28.6	65.3	(10,2)	4	1.0422
13	128	20	2	NS	(−,0)	28.6	65.3	(10,2)	4	1.039
14	256	40	2	NS	(−,0)	28.6	65.3	(10,2)	4	1.0377
					Geometry for a small very sharp riblet					
15	64	10	2	NS	(−,0)	57.1	77.0	(10,2)	4	1.0483
16	256	40	2	NS	(−,0)	57.1	77.0	(10,2)	4	1.0445

Run = Reference run number
N_x = Number of modes in X (streamwise) direction
N_y = Number of modes in Y (wall normal) direction
N_z = Number of modes in Z (cross-flow) direction
ϵ = Measure of Gaussian width (see (6))
BC = Slip (S) or no-slip (NS) (VW = virtual wall) boundary condition below the rib, wire or flat surface
(ξ_1, ξ_2) = Decay constants (see (7))
AR = Domain aspect ratio (height/width)
S^+ = Normalized crest-to-crest spacing
H^+ = Normalized crest height
θ = Rib angle
(α, β) = Force field gains (see (3))
G_{rev} = Magnitude of reverse pressure gradient below rib / pressure gradient above
DR = Drag ratio of riblet side to flat side

TABLE 1. Grid resolution effects

it should be noted that the riblet geometry in Runs 12–14 corresponds, roughly, to the riblet used in one of the fully turbulent cases (§4.1.2). As indicated in table 1 the drag ratio is not particularly sensitive to spatial resolution if enough resolution is used. In each case, quadrupling the resolution from $N_y = 64$ to $N_y = 256$ produces only a small 0.5% drop in the drag ratio. These results are consistent with the trends observed by Choi *et al.* (1991*a*). One thus concludes that the resolution used in the later turbulent flow simulations for which $N_y = 64$ should give sufficient accuracy and that it is reasonable to expect that the turbulent drag that would have been computed with *much* higher spatial resolution would not differ in any substantial amount from the drag results reported here.

Choi *et al.* (1991*a*) found that larger riblets produced greater laminar drag. This

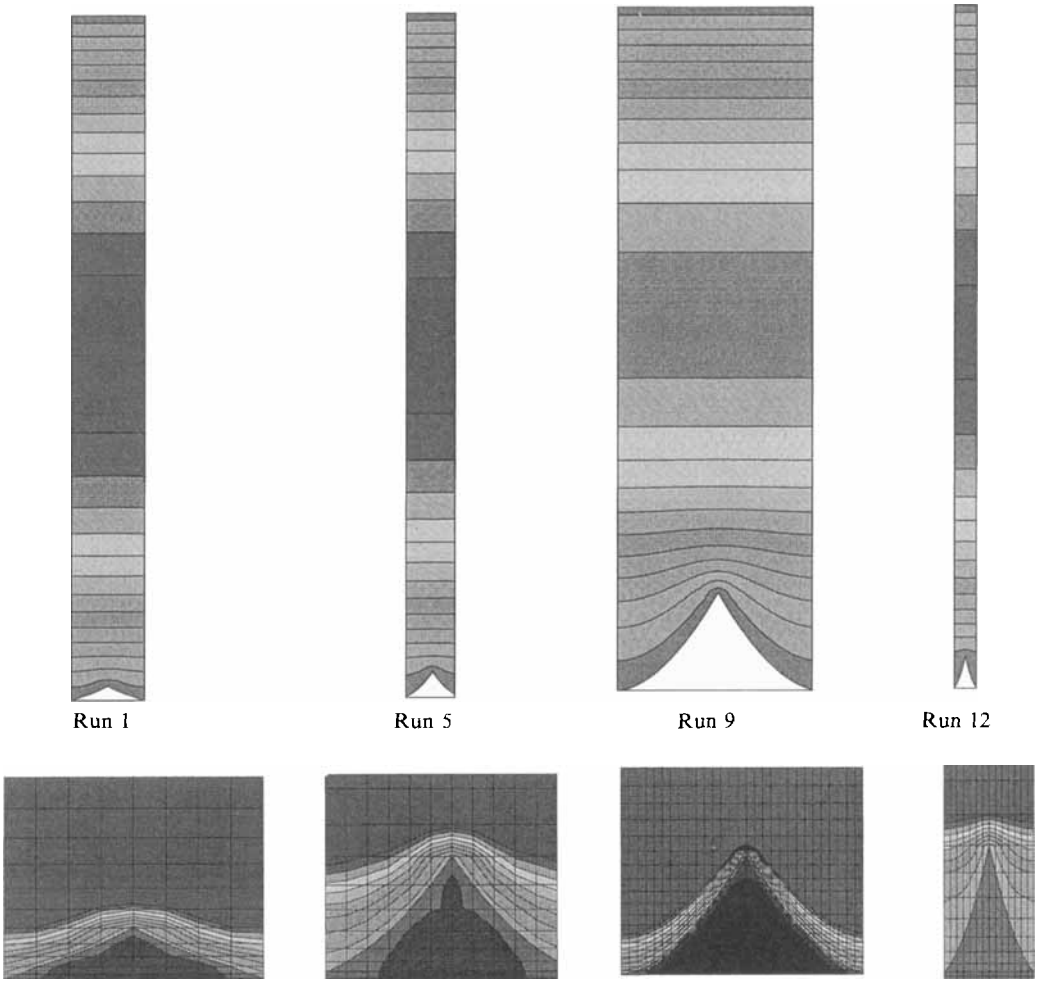

FIGURE 2. Contours of constant U-velocity over select single riblets. Close-up view of riblet region and 3/2 grid are seen below the full channel view.

is an intuitively reasonable result since larger riblets present more surface area. One observes the same trends in table 1: riblets which project further toward the centreline or have larger rib angles (θ) produce greater drag. In no instance did the current laminar simulations give less drag on the riblet side, and this result is consistent with those of Choi *et al.* (1991*a*).

The effects of the three different smoothing techniques are presented in table 2: spectral filtering of the $\boldsymbol{U} \times \boldsymbol{\Omega} + \boldsymbol{f}$ term, forced internal flow below the riblet surface, and spatial smoothing of $\boldsymbol{f}$ in the x- and z-directions. The table presents the effects of these three techniques on a $\theta = 45°$ riblet projecting 14.7% across the channel. For such a rib the drag is about 10% greater than on a flat surface and this provides a more sensitive comparison than is possible with a smaller riblet.

The strength of the spectral smoothing is characterized by the constants ξ_1 and ξ_2 (see (7)). A small value of ξ_1 and a more negative value of ξ_2 both imply stronger smoothing. As seen in runs 17–20, as the strength of spectral smoothing is increased, the drag ratio also increases. The change in drag is caused, at least in part, by the resulting inaccuracy in the determination of the derivative $\mathrm{d}\overline{U}/\mathrm{d}y$ where $\overline{U}$ is the

Run	N_y	N_z	ϵ	BC	(ξ_1, ξ_2)	AR	θ	(α, β)	G_{rev}	DR
Vary spectral smoothing for large rib										
17	64	20	2	NS	(−,0)	3.4	45.0	(10,1)	4	1.1065
18	64	20	2	NS	(20,−1)	3.4	45.0	(10,1)	4	1.1067
19	64	20	2	NS	(5,−10)	3.4	45.0	(10,1)	4	1.1117
20	64	20	2	NS	(2,−10)	3.4	45.0	(10,1)	4	1.141
Vary G_{rev} below large rib										
21	64	20	2	NS	(20,−1)	3.4	45.0	(10,1)	0	1.1072
22	64	20	2	NS	(20,−1)	3.4	45.0	(10,1)	4	1.1067
23	64	20	2	NS	(20,−1)	3.4	45.0	(10,1)	100	1.093
24	64	20	2	NS	(20,−1)	3.4	45.0	(10,1)	4–800†	1.1066
Vary width of Gaussian spatial smoothing for large rib										
25	64	20	1	NS	(−,0)	3.4	45.0	(10,1)	4	1.1086
26	64	20	2	NS	(−,0)	3.4	45.0	(10,1)	4	1.1065
27	64	20	10	NS	(−,0)	3.4	45.0	(10,1)	4	1.1049

† G_{rev} was $4G$ under the crest and varied smoothly to $800G$ under the bottom of the valley

TABLE 2. Different smoothing technique effects

mean streamwise velocity on the opposing flat wall. Note, however, that there is virtually no difference (0.02%) in DR between the no-smoothing case (run 17) and the mild smoothing case (20th order smoothing, run 18). The mild smoothing of run 18 is the same as that used in the turbulent simulations over riblets (§4). Even the strongly smoothed cases (runs 19 and 20) produced remarkably good drag results (a few percent different from the unsmoothed case).

The creation of flow below the solid riblet surface, so that the velocity profile is reasonably smooth across the surface, provides an additional method of smoothing. To explore the solution sensitivity to this internal flow, the amplitude of G_{rev} is varied from zero to $-100G$ in runs 21–23. It is evident that the difference in the drag ratio between no forcing ($G_{rev} = 0$) and mild forcing is only 0.1% while a much larger forcing ($-100G$) only produces an 0.8% change in the drag ratio. For these three simulations G_{rev} is a constant everywhere below the rib surface whereas in the turbulent simulations G_{rev} was made to be small below the riblet peaks and large below the valleys in order to better smooth the mean velocity over each section. In run 24 G_{rev} is $-800G$ below the valley portion and drops to $-4G$ below the rib crest. The effect of G_{rev} upon the drag of a riblet is again negligible. It is seen from runs 21–24 that the effect of G_{rev} upon the drag is small and that the force field used to create the riblet itself effectively decouples the flows on either side.

In practice a slight spatial smoothing of the force field is used. As seen in the results from runs 25–27, if the exponential constant (ϵ) used in the Gaussian spatial smoothing (see (6)) is varied from -10 to -1 ($\epsilon = -10$ means virtually no smoothing whereas $\epsilon = -1$ implies spreading the force field widely to ± 2 grid sites) there is only a 0.5% change in the drag ratio. The width of the Gaussian used in the turbulent simulations of flow over riblets (§§4.1.1, 4.1.2) is intermediate ($\epsilon = -2$, $\boldsymbol{f}$ spread approximately to ± 1 grid site) and thus is expected to produce an error in the drag of around 0.2%.

We obtain second-order convergence near the surface. However, the cosine grid is very fine near the surface and such accuracy is adequate to ensure small errors in that

Run	N_y	N_z	ϵ	BC	(ξ_1, ξ_2)	AR	θ	(α, β)	G_{rev}	DR
Check effect of slip/no-slip below large rib										
28	64	20	2	NS	(20,−1)	3.4	45.0	(10,1)	4	1.1067
29	64	20	2	S	(20,−1)	3.4	45.0	(10,1)	4	1.1064
Check effect of gap in valley of large rib										
30	64	20	2	S	(20,−1)	3.4	45.0	(10,1)	4	1.1064
31	64	20	2	S	(20,−1)	3.4	45.0	(10,1)	4	1.1067(Gap)

TABLE 3. Other comparisons

region as demonstrated by the laminar calculations. Elsewhere in the flow no spatial smoothing is applied, only the high-order spectral filter.

The conclusion to be drawn from these sensitivity checks is that, if the turbulent drag is affected by these various parameters as it is in the laminar case, the turbulent drag results to be presented below are computed with sufficient spatial resolution and are insensitive to the smoothing used. That is, the sum of the absolute values of the various possible resolution and smoothing errors in drag ratio in the turbulent runs amounts to only about 1%.

3.2.2. *Boundary condition tests for laminar flow over riblets*

Simulations to verify the adequacy of the boundary conditions used below the riblet surface and one other test were also performed. The first test was to compare the drag ratio for two riblets having either a no-slip (run 28) or free-slip (run 29) boundary condition imposed on the flow domain boundary below the riblet. As seen in table 3, there is virtually no effect (0.03%) upon the drag. In the turbulent simulations a free-slip boundary condition is used.

In the turbulent simulations a small kink or gap is permitted in the riblet shape deep in the valley between ribs (see §4.1.1). That is, in a valley the j_s locations of the frozen grid sites were ...7 6 5 4 2 2 4 5 6 7... or ...7 6 5 4 2 4 5 6 7...: there is a kink between sites at $j_s = 2$ and $j_s = 4$. The kink permits the use of specific riblet dimensions and numbers of riblets within the constraints imposed by the domain size in x and z and the desired grid resolution. In runs 30 and 31 a comparison is made between the drag ratios found with a smooth valley ($j_s = \ldots 5\ 4\ 3\ 2\ 3\ 4\ 5\ldots$) and a valley with a small kink ($j_s = \ldots 5\ 4\ 2\ 2\ 2\ 4\ 5\ldots$). There is again only a minor (0.03%) change in the drag ratio. This is reasonable since the kink is deep in the slow valley flow where wall-normal velocity gradients are very small.

3.2.3. *Turbulent flow over a virtual flat plate*

An important test of the virtual surface approach is to determine whether a virtual no-slip boundary can accurately represent an exact no-slip boundary for the case of fully turbulent flow. For this purpose, two simulations of fully developed turbulence, which are described in table 4 as runs 32 and 33, were performed. In the first (run 32), the flow was bounded on one side by a no-slip boundary generated by directly imposing the no-slip boundary conditions (i.e. an exact no-slip boundary on which $\boldsymbol{U} = 0$) and on the other by a virtual surface generated by methods described in §2. This simulation allows for a direct comparison of the turbulence statistics near both walls. Such a comparison, while necessary, is not sufficient to eliminate the possible existence of global errors. To determine such numerical effects, a second simulation (run 33) was performed in which the exact no-slip boundary conditions were imposed

Run	N_x	N_y	N_z	ϵ	BC	(ξ_1, ξ_2)	S^+	H^+	θ	(α, β)	G_{rev}	DR
						Modelled flat plate						
32	48	97	64	2	S	(20,−1)	NA	NA	NA	(37.5,15)	1	1.001±0.023
						Real flat plate						
33	48	97	64	NA	NS	NA	NA	NA	NA	NA	NA	NA
						Fully modelled riblets						
34(Case 1)	48	65	128	2	S	(20,−1)	18	5.3	30.0	(285,0.04)	4–800	0.978±0.019
35(Case 2)	48	65	256	2	S	(20,−1)	11.7	9.4	58.0	(500,5)	4–800	0.967±0.023
						Cross-flow damping modelled 'wires'						
36	48	65	64	1	NS	(20,−1)	18.4	5.1	29.0	(0,5)	NA	0.792±0.017
37	48	65	64	1	NS/VW	(20,−1)	24.1	4.97	22.4	(0,5)	NA	0.817±0.015
38	48	65	64	1	NS	(20,−1)	36.5	5.03	15.4	(0,5)	NA	0.868±0.012
39	48	65	64	1	NS	(20,−1)	5.82	4.81	58.8	(0,5)	NA	0.728±0.034
40	48	65	64	1	NS	(20,−1)	11.9	4.92	39.6	(0,5)	NA	0.74 ±0.012
41	48	65	64	1	NS	(20,−1)	76.3	5.25	7.8	(0,5)	NA	0.943±0.014
42	48	65	64	1	NS	(20,−1)	154.2	5.31	3.9	(0,5)	NA	0.99 ±0.028
43	48	65	64	1	NS	(20,−1)	37.7	5.19	15.4	(0,1)	NA	0.922±0.015
44	48	65	64	1	NS	(20,−1)	38.2	2.32	6.9	(0,5)	NA	0.934±0.018
45	48	65	64	1	NS	(20,−1)	38.2	9.29	26.1	(0,5)	NA	0.906±0.0093
46	48	65	64	1	NS	(20,−1)	39.4	0.61	1.8	(0,5)	NA	1.006±0.014
47	48	65	64	1	NS	(20,−1)	39.4	14.8	36.3	(0,5)	NA	0.995±0.014
48	48	65	64	1	NS	(20,−1)	37.5	7.02	20.5	(0,5)	NA	0.863±0.013
49	48	65	64	1	NS	(20,−1)	39.2	21.1	47.1	(0,5)	NA	0.991±0.012
50	48	65	64	1	NS	(20,−1)	36.5	5.03	15.4	(0,10)	NA	0.863±0.0121
51	48	65	64	1	NS	(20,−1)	38.1	5.25	15.4	(0,3)	NA	0.905±0.016
52	48	65	64	1	NS	(20,−1)	5.93	4.91	58.8	(0,5)	NA	0.714±0.012
						Cross-flow damping modelled 'fences'						
53	48	65	64	2	NS	(20,−3)	18.04	4.97	28.8	(0,5)	NA	0.773±0.014
54	48	65	96	2	NS	(20,−3)	3.88	4.81	68.0	(0,5)	NA	0.729±0.012
55	48	65	64	2	NS	(20,−3)	37.7	5.2	15.4	(0,5)	NA	0.875±0.013
56	48	65	64	2	NS	(20,−3)	34.5	13.03	37.1	(0,5)	NA	0.669±0.012
						'Real' wire model						
57	48	65	64	2	NS	(20,−3)	40.5	5.6	15.5	(286,5)	NA	1.0496±0.016

TABLE 4. Turbulence simulations

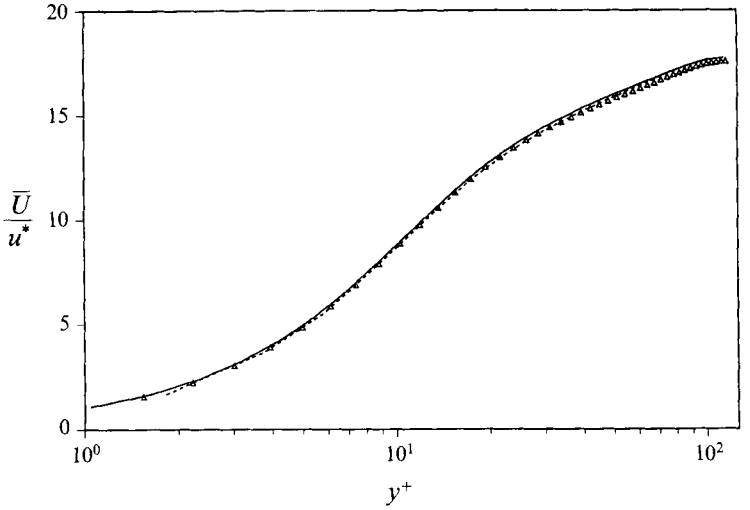

FIGURE 3. Mean streamwise velocity, $\overline{U}$, for turbulent flow runs 32 and 33. - - -, virtual wall; ——, opposing real boundary (run 32); △, both real boundaries from run 33.

on both walls (i.e. no virtual wall was present). This simulation was performed at the same friction Reynolds number, R^*, as run 32. Unless otherwise stated, $\overline{U}$ denotes the mean velocity, u', v', and w' indicate root mean square velocities while u, v, and w indicate fluctuating quantities (e.g. $u = U - \overline{U}$). Again, (U, V, W) indicate the total velocity as in equation (1). In addition, length scales made non-dimensional by the viscous scale l^*, where $l^* \equiv \nu/u^*$, will be denoted by, for example, $y^+ \equiv y/l^*$. Each simulation was run to a steady state before statistics were accumulated.

In run 32, the virtual wall was located 15 grid points above the boundary of the computational domain and the dimensions of the domain were 1217, 231, and 609 in units of l^* in the x-, y- and z-directions respectively. In run 33 the dimensions were 1155, 231, and 577. The time step used in both cases is $\Delta t u^{*2}/\nu = 0.043$. The control parameters, α and β, for run 32 were 37.5 and 15, respectively. These parameters were fine-tuned (maximized) before the longer simulations were performed to ensure a very close approximation to no-slip conditions at the virtual wall.

Certain differences in scaling for runs 32 and 33 should be noted. For example, in run 32 the height of the computational domain is larger than the distance between virtual and exact walls whereas for run 33 the walls coincide exactly with the domain. This leads to the definition of the friction Reynolds number in these two simulations as $R^* = u^* H/\nu$, where u^* is the friction velocity based on the total force driving the flow between virtual (or exact as in run 33) and exact walls, and H is half the distance between the walls. Based on this definition R^* was chosen to be 115 for both simulations. The differences in scaling between runs 32 and 33 are somewhat subtle and have been fully taken into account in all statistical comparisons to be presented in this section.

Other differences between run 32 and run 33 exist. The streamwise and spanwise spatial resolution for run 33, measured in units of l^*, is about 5% greater than the resolution in run 32. The resolution in the y direction for run 32 is greater in the vicinity of the exact no-slip wall compared to the resolution near the virtual wall because of the uneven grid distribution in the wall-normal direction. The total integration time for run 32 ($T^+ = 1733$ where $T^+ = N_{step}\Delta t u^{*2}/\nu$, and $N_{step}\Delta t$ is the computational time) is twice that for run 33 ($T^+ = 867$) where results from both

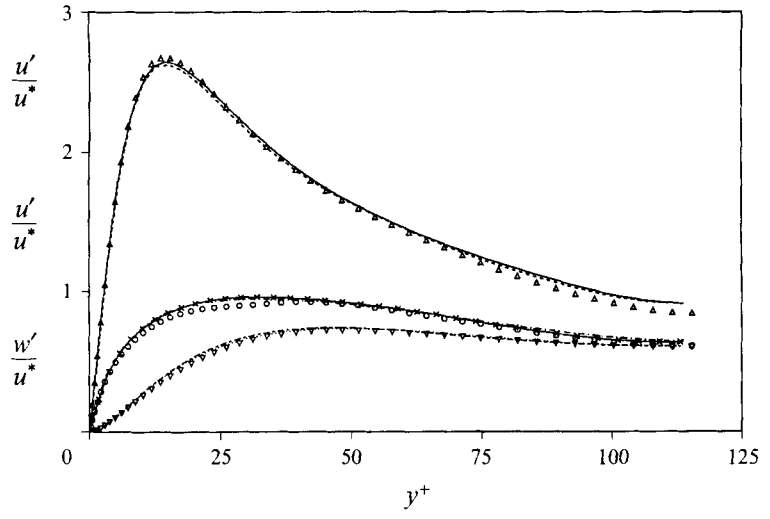

FIGURE 4. Fluctuating velocity profiles. ——, u'/u^*, real wall, run 32; - - -, u'/u^*, virtual wall; △, u'/u^*, real walls, run 33; ..., v'/u^*, real wall, run 32; – – – –, v'/u^*, virtual wall; ▽, v'/u^*, real walls, run 33; — · — · —, w'/u^*, real wall, run 32; -×-×-×-, w'/u^*, virtual wall; ○, w'/u^*, real walls, run 33.

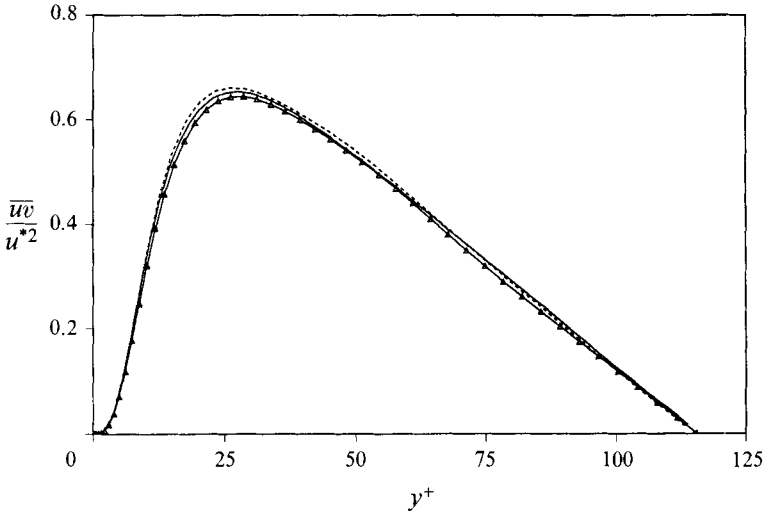

FIGURE 5. Reynolds stress profiles. - - -, virtual wall; ——, opposing real boundary (run 32); △, both real boundaries from run 33.

sides of the channel are averaged giving a sampling error which is roughly equal to that of run 32. It is straightforward to estimate the large eddy turnover time for this flow, T_e, by $T_e = 2H/(u')_{max}$, where $(u')_{max}$ is an estimate for the maximum root mean square streamwise turbulence intensity. For these flows, $T_e u^{*2}/\nu \simeq 77$, so that run 32 represents about 23 large-eddy turnover times.

Plots of the mean velocity profiles for both runs are shown in figure 3. The profiles for the virtual wall and the opposing exact wall are in good agreement, both exhibiting a logarithmic layer yielding a von Kármán constant of 0.4. In addition, the velocity profile for run 33 is in good agreement with those of run 32. For runs 32 and 33 the ratios R_{cl}/R_b, where R_{cl} and R_b are Reynolds numbers based on the centreline and bulk velocities respectively, are 1.9, in reasonable agreement with 1.7 obtained

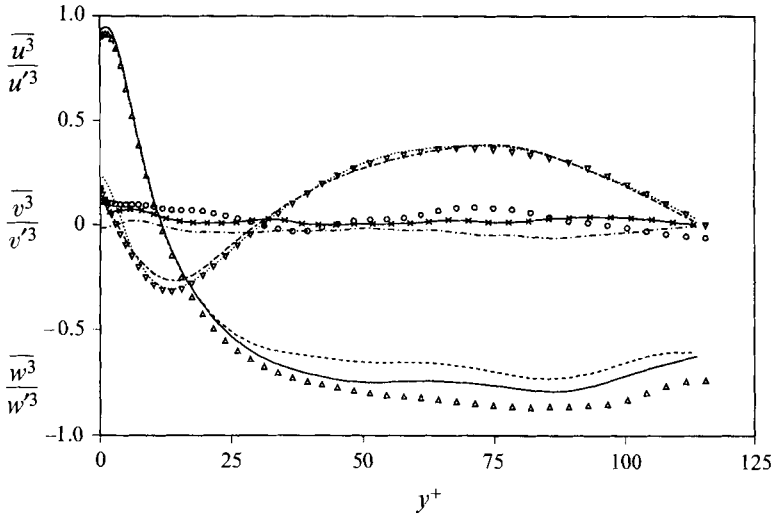

FIGURE 6. Skewness. ——, $\overline{u^3}/u'^3$, real wall, run 32; - - -, $\overline{u^3}/u'^3$, virtual wall; △, $\overline{u^3}/u'^3$, real walls, run 33; ····, $\overline{v^3}/v'^3$, real wall, run 32; – – – –, $\overline{v^3}/v'^3$, virtual wall; ▽, $\overline{v^3}/v'^3$, real walls, run 33; — · — · —, $\overline{w^3}/w'^3$, real wall, run 32; —×—×—, $\overline{w^3}/w'^3$, virtual wall; ○, $\overline{w^3}/w'^3$, real walls, run 33.

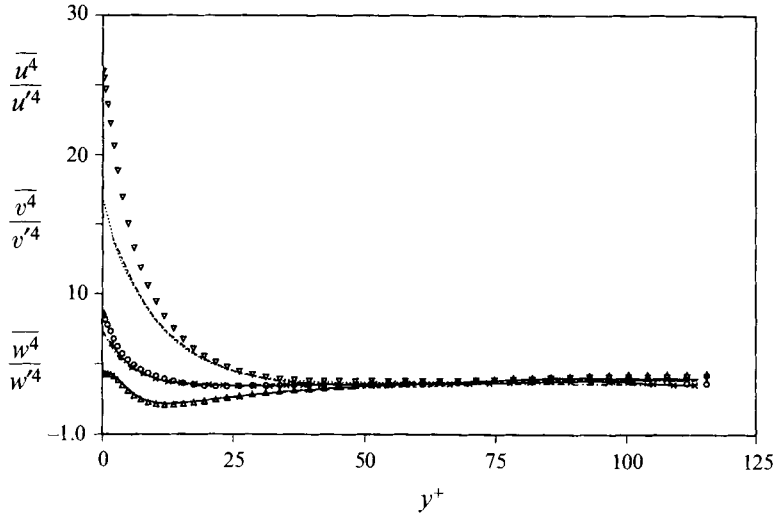

FIGURE 7. Flatness. ——, $\overline{u^4}/u'^4$, real wall, run 32; - - -, $\overline{u^4}/u'^4$, virtual wall; △, $\overline{u^4}/u'^4$, real walls, run 33; ····, $\overline{v^4}/v'^4$, real wall, run 32; – – – –, $\overline{v^4}/v'^4$, virtual wall; ▽, $\overline{v^4}/v'^4$, real walls, run 33; — · — · —, $\overline{w^4}/w'^4$, real wall, run 32; —×—×—, $\overline{w^4}/w'^4$, virtual wall; ○, $\overline{w^4}/w'^4$, real walls, run 33.

from the experimental correlations of Dean (1978). The turbulence intensities scaled with the friction velocity u^* are shown in figure 4. It is evident that the agreement between the virtual wall and the opposing exact no-slip wall (run 32) is excellent as is the agreement between run 32 and run 33. The Reynolds shear stress profiles for these two simulations are shown in figure 5 and also indicate good agreement for all three walls. The minor discrepancies evident in these results can easily be accounted for by sampling error considerations.

The higher-order statistics, skewness and flatness, normalized by local root-mean-square values, are shown in figures 6 and 7. The skewness results for all three walls

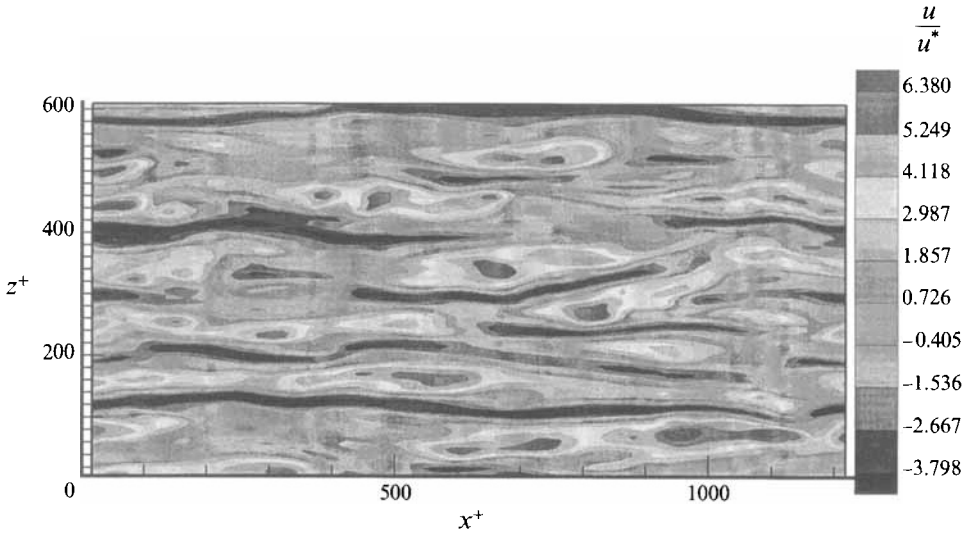

FIGURE 8. Contour plot of of streamwise velocity, u/u^* on an (x, y)-plane at $y^+ = 10.23$ above the virtual wall in run 32.

are in good agreement and again it can be shown that the minor differences are well within the bounds of the sampling error. The flatness results show excellent agreement for all three walls for the spanwise and streamwise velocity components. Near the wall, for $y^+ < 15$, it is evident that the flatness for the vertical velocity fluctuations in run 33 is higher than for the virtual wall results. Some part of this difference is probably due to sampling errors, since, for example, the results of Kim *et al.* (1987) give a value of about 22 for the flatness for v very near the wall which is roughly halfway between the results for run 32 and run 33. Sampling errors may not account for the entire difference between these two cases for the flatness and it is possible that that small errors in satisfying the condition of no flow normal to the virtual surface could be a contributing factor.

Figure 8 is a contour plot of the streamwise velocity component in the horizontal (x, z)-plane at a distance of $y^+ = 10.23$ above the virtual surface. The well-known low-speed streaky structure is clearly evident in the figure. The positive skewness which is expected at this height is also evident. A quantitative measure of the spanwise length scale defined by the streaks, λ^+, can be determined by computing the correlation

$$R_{uu}(\Delta z) = \frac{\overline{u(x, y, z)u(x, y, z + \Delta z)}}{u'^2} \tag{8}$$

and using the definition that the streak spacing is twice the spanwise distance at which $R_{uu}(\Delta z)$ attains a minimum. For the virtual wall this analysis yields $\lambda^+ = 95$ at $y^+ = 6.1$ and 114 at $y^+ = 20.3$. These values are within the experimental range and are in agreement with the observation that the streak spacing increases with increasing distance from the wall (Shraub & Kline 1965; Smith & Metzler 1983; Sirovich *et al.* 1991).

In figure 9 a section of the same flow in a (y, z)-plane in which the velocity vectors in the plane are superimposed on contours of the streamwise velocity is shown. It is evident in this instantaneous snapshot that there are no qualitative differences between the structure above the virtual wall and the exact no-slip wall. The up-welling of low-speed fluid and down-welling of high-speed fluid is evident on both walls in the vicinity

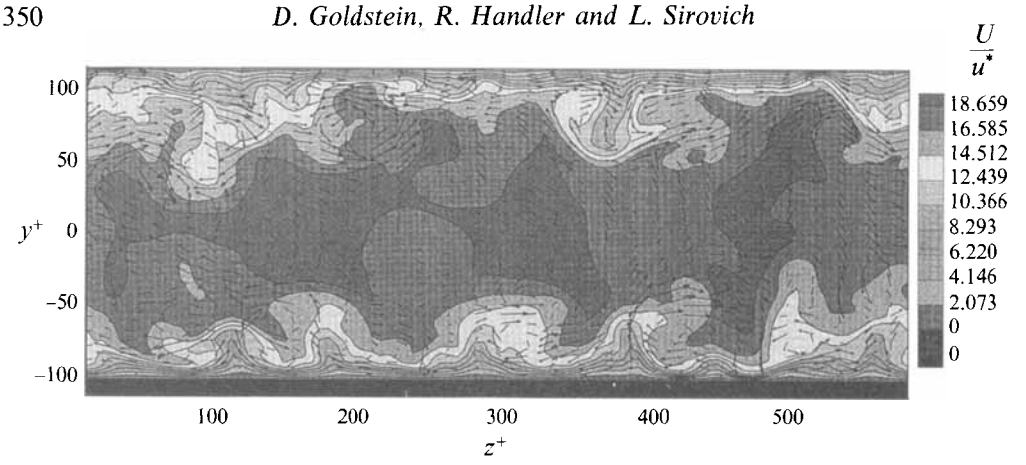

FIGURE 9. View looking down the channel in the x-direction showing contours of constant streamwise (U) velocity and selected V, W velocity vectors. Top boundary is smooth no-slip; bottom boundary is a virtual flat surface. Note that a weak back-flow exists below the virtual surface.

of quasi-streamwise-oriented structures which are known to persist near the wall (Robinson 1991; Brooke & Hanratty 1993; and Bernard, Thomas & Handler 1993).

The main conclusion from these two simulations is that the statistics of the turbulence above a virtual wall are almost indistinguishable from those above an exact no-slip boundary. Furthermore, the structure of the turbulence found near the the virtual wall shows excellent agreement with the structure found experimentally. In particular the characteristic length scale associated with wall-bounded turbulence – the 100 wall unit scale associated with the wall layer streaks – is reproduced above the virtual wall. Though some minor discrepancies between run 32 and run 33 were noted, these differences are at least in part due to sampling errors and do not indicate any fundamental problems with the virtual wall approach. These detailed numerical tests for both laminar and turbulent flows (§§3.2.1 and 3.2.2) indicate that the virtual no slip wall is a thoroughly sound and robust model for the exact no-slip boundary conditions.

4. Results for simulations over riblets and modelled riblets

4.1. *Turbulent flow over riblets*

For the two simulations of turbulent flow over riblets we expect relatively small drag reductions. Riblets having a triangular or cusped U cross-section, a peak to peak spacing, S^+, of 10 to 20, and a height, H^+, of 5 to 15 are found experimentally to be most effective (Walsh 1990) in reducing drag. The channel modelled here has the orientation given in figure 10. In the bulk of the domain between the ribbed surface and the top boundary a constant pressure gradient, G, is applied in the x-direction. The value for G is chosen so as to achieve a steady-state value of R^* (≈ 125).

Accurate simulation of flow over riblets requires that each rib cross-section be represented by at least several grid points. In addition, to accurately simulate the turbulent flow the channel width and length should be greater than the size of characteristic turbulent flow structures such as boundary layer streaks and quasi-streamwise vortices. Jimenez & Moin (1991) suggest that a minimum channel for modelling sustained turbulence (i.e. one streak per wall) has a length of roughly $L_x^+ = 250$–350 and a width of $L_z^+ = 100$. Since their conclusions are based on simulations over flat walls, and since *a priori* domain size estimates may not apply for

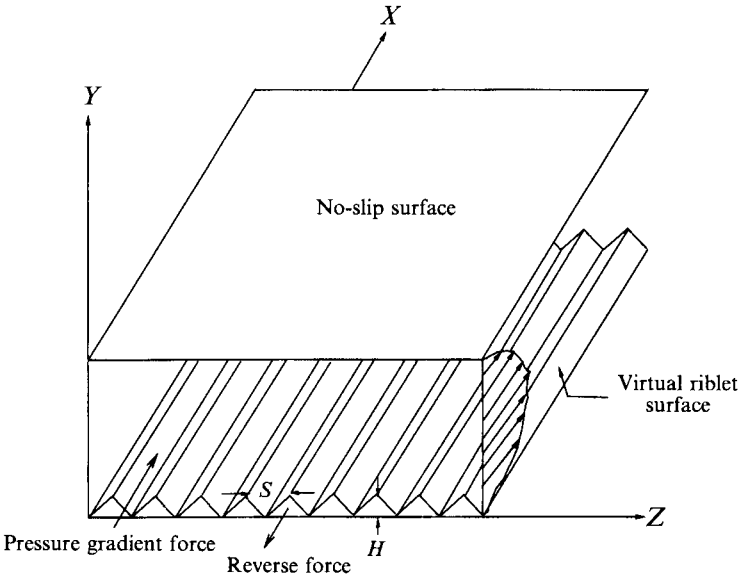

FIGURE 10. Geometry for flow simulation of channel bounded by two impermeable boundaries and containing a virtual riblet surface.

a ribbed wall, domain dimensions of 1250:250:375 (viscous units) in x:y:z are chosen as safe estimates, and are likely to be sufficient to capture the dominant flow physics. Because of the severe resolution and temporal requirements implied by this analysis, it has not been feasible to perform detailed grid resolution studies of turbulent flow over riblets.

In this investigation we present detailed flow results for two different riblet configurations using two different spanwise resolutions. Both configurations place the rib dimensions within the drag reducing regime. In Case 1 (run 34 in table 4) the ribs are short and squat, $S^+ = 18$ and $H^+ = 5.3$, and in Case 2 (run 35) the ribs are higher and more closely spaced, as in the laminar runs 12–14, with $S^+ = 11.7$ and $H^+ = 9.4$.

4.1.1. *Case 1 ($S^+ = 18$, $H^+ = 5.3$)*

In the first simulation the riblets are fairly widely spaced and do not protrude far into the flow. The grid sites in the y-direction which define the riblet geometry are given (for successive spanwise (z) locations) by ...2 2 4 5 6 7 6 5 4 2 2... These points lie on the expanded (in x and z) 3/2 grid which has the cosine scaling given previously (§3.2.1). The peak-to-peak spacing of the ribs is 9 expanded-grid sites (in z or 6 regular grid sites) and the ribs are 6 regular grid sites (in y) high. In this case there are 21 riblets along the channel width.

The lower flow field boundary is shear free and there is a small space between the boundary and the riblet no-slip surface. In this space a force in the $-x$-direction, G_{rev}, as described in §3, is applied to create a flow inside the ribs that reduces the kinks that otherwise develop in the mean velocity profile. The value of G_{rev} is small ($-4G$) below the rib peaks and large ($-800G$) below the valleys. The G_{rev} profile was chosen to minimize the energy in the highest Chebyshev mode for $\overline{U}$ over each portion of the rib. Once this procedure was complete and the oscillations were very small, it was found that the moderate spectral smoothing described earlier was sufficient to eliminate the remaining oscillations. The simulation begins by abruptly inserting the ribbed virtual surface into an equilibrium turbulent channel flow and allowing the

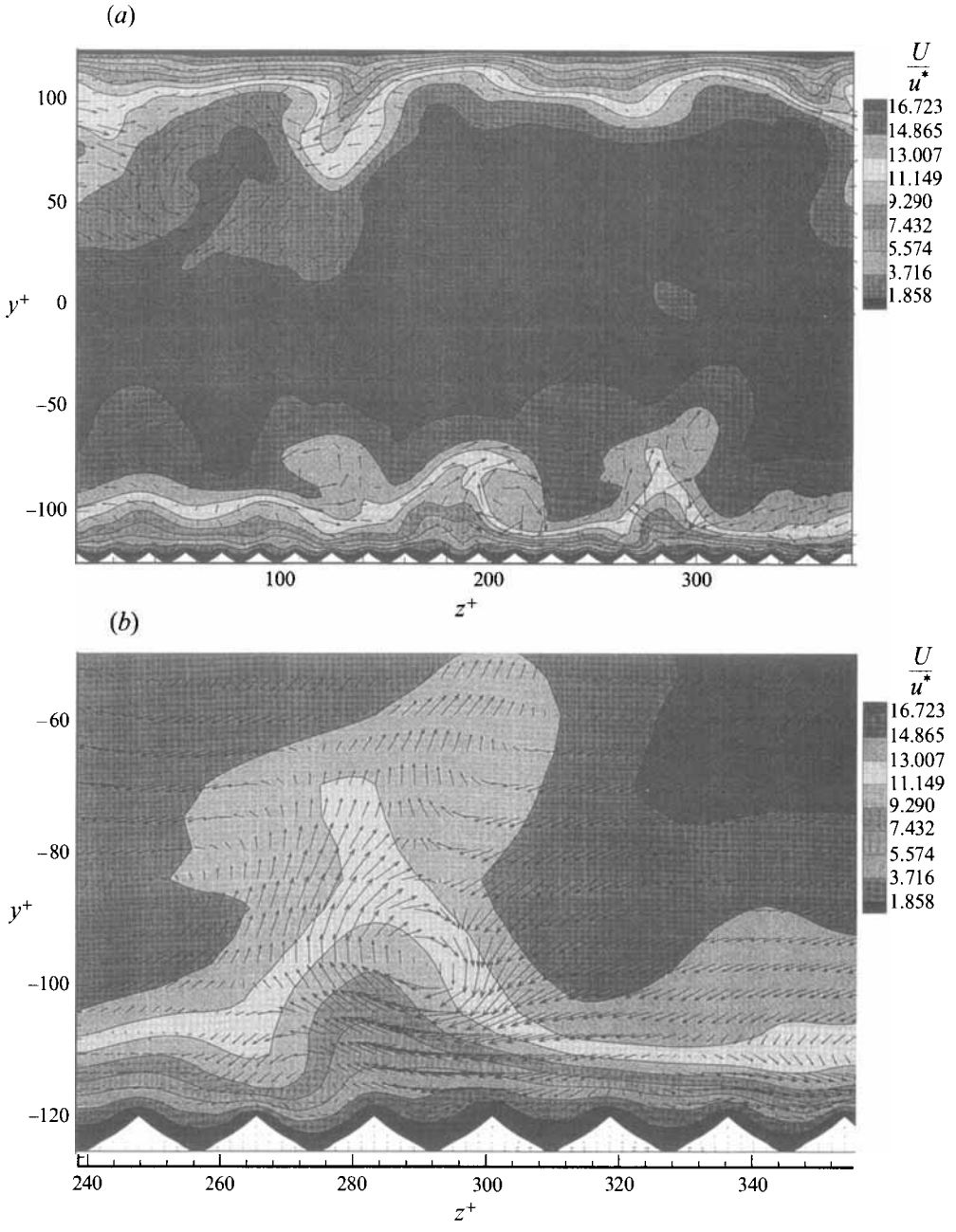

FIGURE 11. (*a*) View looking down the channel in the x-direction showing contours of constant streamwise (U) velocity and selected V, W velocity vectors. Top boundary is smooth no-slip; bottom boundary has wide (Case 1) riblets. (*b*) Close-up view of a portion of (*a*).

flow to relax for at least one large-eddy turnover time. The autocorrelation of the ratio of the drag on the ribbed side to the smooth side was used to estimate the number of time steps between independent flow field realizations. In the present case, the simulation was run for about 23 such independent realizations.

Typical instantaneous results are shown in in figure 11(*a,b*) which gives views

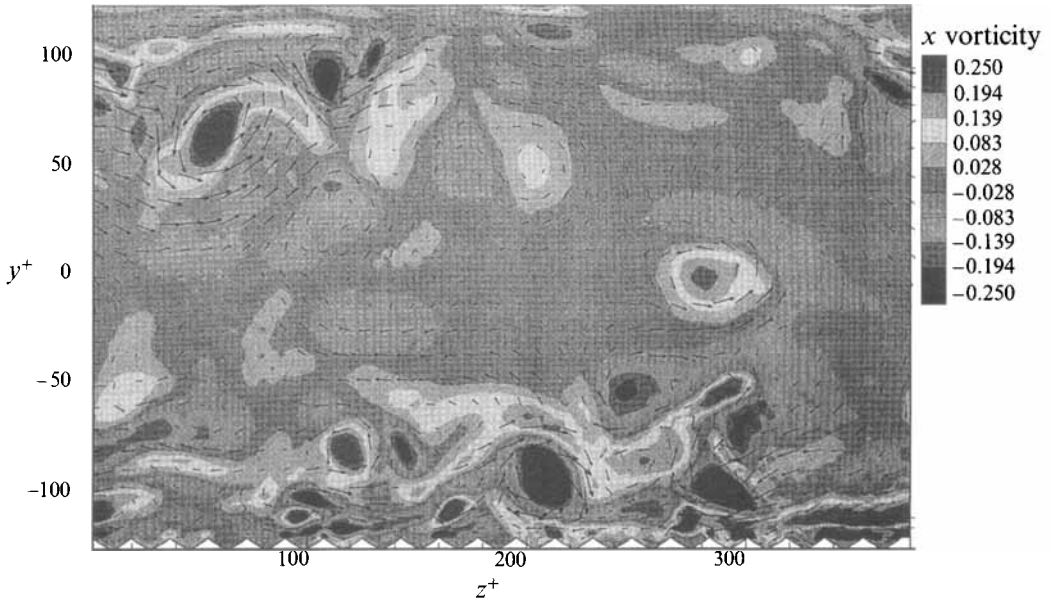

FIGURE 12. View looking down the channel in the x-direction showing contours of constant streamwise (x) vorticity and selected V, W velocity vectors.

looking down the channel in the x-direction. Contours of constant streamwise velocity are shown along with vector velocities in the (y, z)-plane. One observes what appears to be ordinary turbulent channel flow in the bulk of the domain indicated by streamwise vortices which draw slow-moving fluid away from the walls and bring high speed fluid toward the walls. A detailed picture of the flow (in figure 11*b*) shows that the ribs seem to affect only the region close to the wall. As expected, near the rib peaks the contours are closely spaced and the velocity gradient (hence drag) is high while in rib valleys the gradient is low. It should be noted that the ribs, essentially defined by the zero velocity contour line, are of a consistently uniform shape even though each is experiencing a different local flow. The rib shapes remain rigid and none are substantially distorted. Hence, the force field is responding sufficiently rapidly to the unsteady flow.

There do occasionally exist small scale streamwise rollers in the riblet valleys. In particular, there is a small roller seen in the riblet valley located around $z^+ = 275$ in figure 11(*b*). In that figure two re-attachment events on rib crests (at $z^+ = 265$ and $z^+ = 318$) and one rib crest separation event ($z^+ = 284$) are evident. Such re-attachment and separation events most often occur at rib crests; hence, the crests tend to pin down and discretize the events in the spanwise direction. The extent to which the vorticity penetrates into the valleys is seen in figure 12 in which contours of constant streamwise vorticity (Ω_x) are shown. For these widely spaced riblets, x-vorticity is seen to sometimes penetrate into valleys but is also often concentrated near riblet crests. Contour plots of flow in (x, z)-planes (figures 13 and 14) clearly show the long low-speed streaks present near both the flat and the ribbed surfaces.

The turbulence intensities and mean velocity profiles above the ribs at both peaks and valleys (figure 15*a–c*) are compared to those obtained from normal flat-walled channel flow (Handler *et al.* 1989). It should be noted that a careful comparison of the turbulence statistics on the flat side of the channel for both runs 34 and 35 with

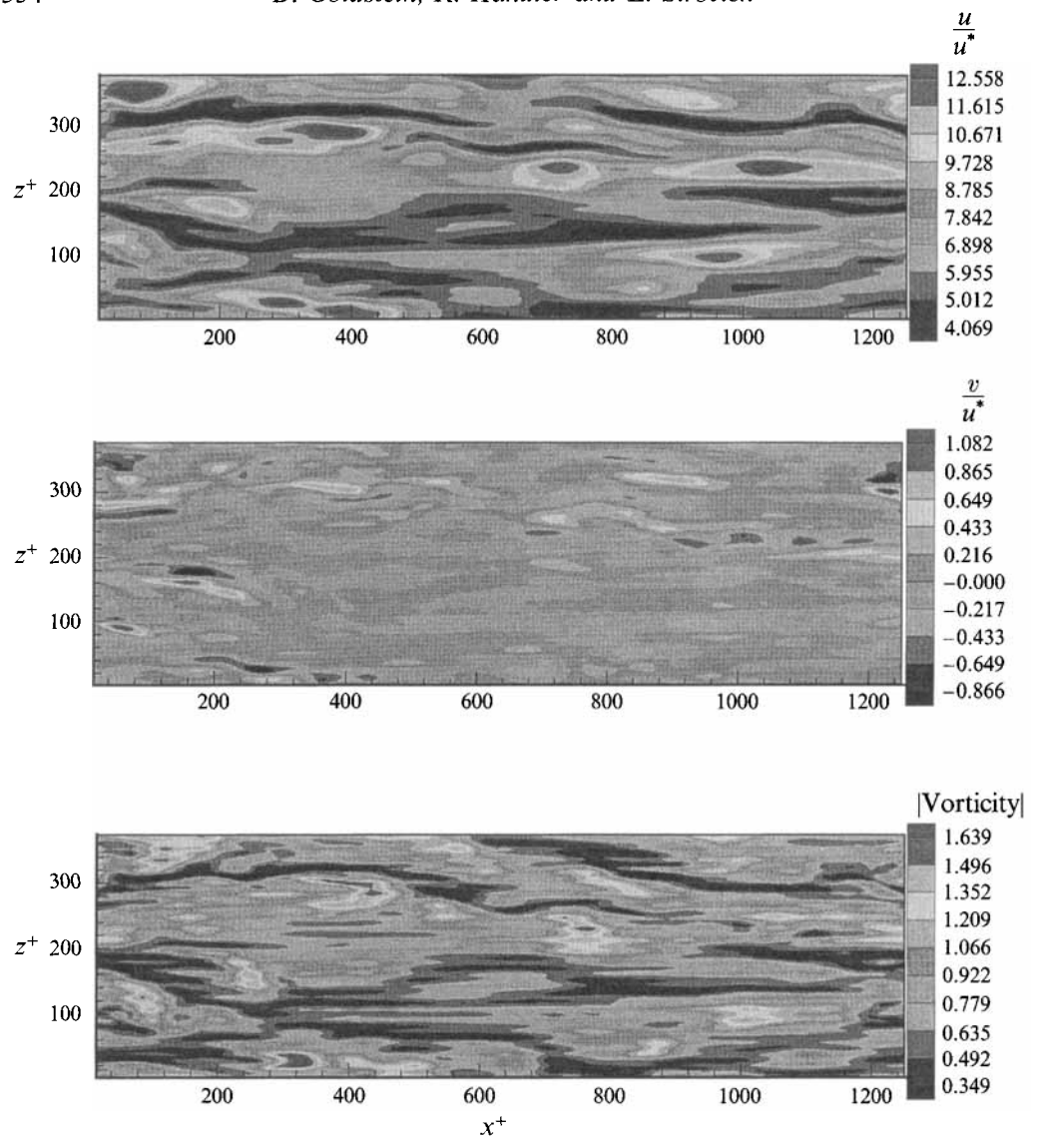

FIGURE 13. Contour plots of an (x, z)-plane at $y^+ = 12$ above the riblet valleys. (*a*) Streamwise velocity, u/u^*, (*b*) wall-normal velocity, v/u^*, and (*c*) magnitude of vorticity, $|\boldsymbol{\Omega}|\nu/u^{*2}$.

the results of Handler *et al.* (1989) show excellent agreement. In figure 15(*a–c*) the corresponding profiles are normalized by the appropriate u^* and l^* for that side. For example, the friction velocity of the ribbed side, u^*_{rib}, can found from the smooth side value, u^*_{smooth}, by using $u^*_{rib} = u^*_{smooth}(DR)^{1/2}$. It is evident that all of the profiles are shifted away from the wall by nearly the height ($5.3l^*$) of the riblet peaks. In figure 16(*a–c*) the profiles are offset wallward by the height of the riblet peak and it is evident that these shifted profiles correspond well with the flat wall results. The riblets appear to push the mean location of the no-slip surface further into the flow. This feature was also observed in the experiments of Vukoslavcevic, Wallace & Balint (1992) and was discussed in Wallace & Balint (1988). The height of the origin, however, is different over the peaks and valleys. A general method for predicting

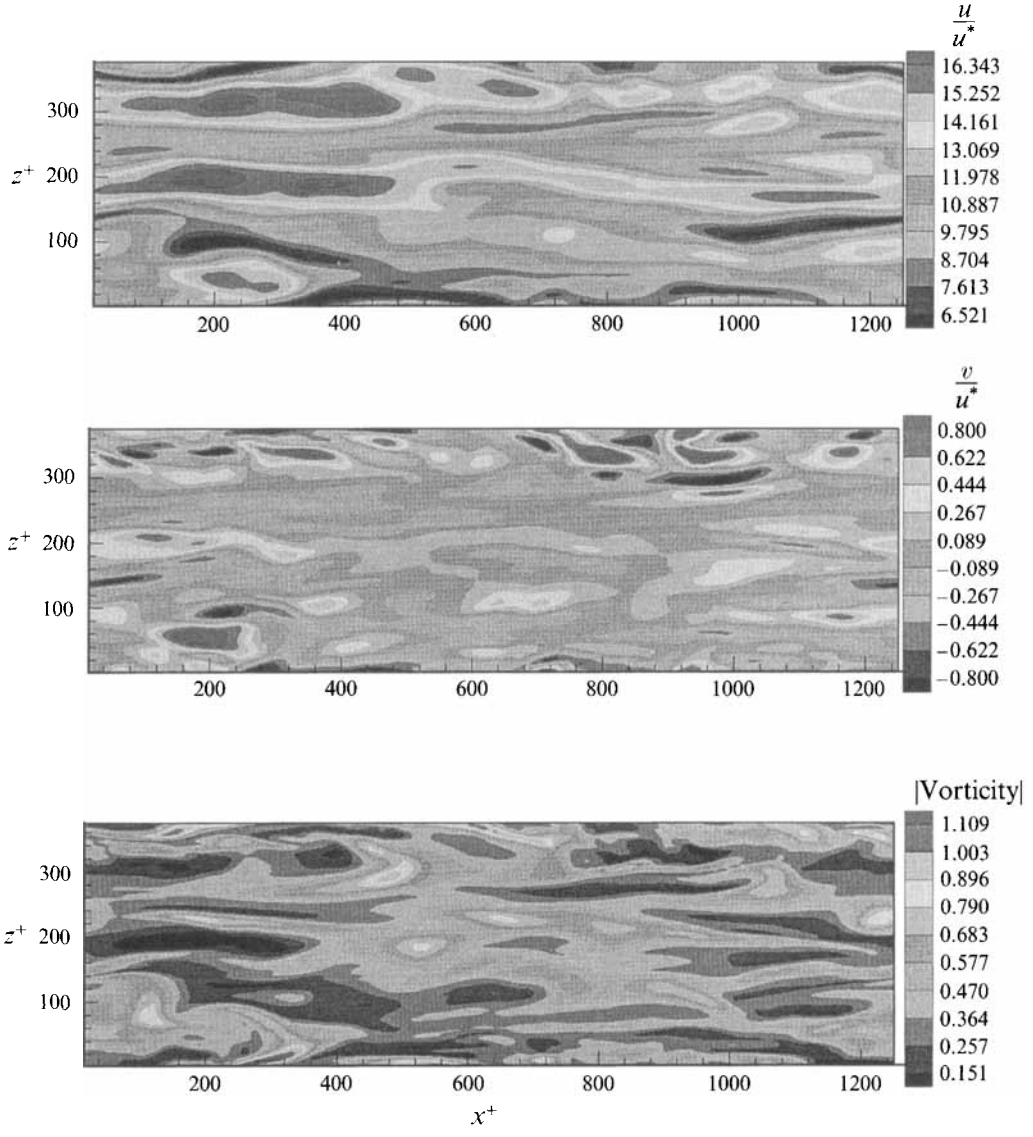

FIGURE 14. Contour plots of an (x, z)-plane at $y^+ = 18$ above the opposing flat real boundary. (*a*) Streamwise velocity, u/u^*, (*b*) wall-normal velocity, v/u^*, and (*c*) magnitude of vorticity, $|\boldsymbol{\Omega}|\nu/u^{*2}$.

the displacement of the origin of the mean velocity profile is not yet evident. In this particular case, however, it appears that in the bulk of the flow the height of the origin is about equal to the peak height. Observe in figure 15(*b*) that over the rib peak the mean velocity profile seems to end abruptly in the buffer region ($5 < y^+ < 30$) with little or no laminar sub-layer. This seems to be simply a consequence of the convex curvature of the riblet crests.

In general, there appears to be little difference between the profiles over the riblets and over a flat plate; the peaks in the Reynolds shear stress, u', and v' are of essentially the same magnitude over both surfaces while the w' peak over the riblets is depressed by a few percent. Note that whereas over a flat surface and over the rib peaks $\mathrm{d}u'/\mathrm{d}y$

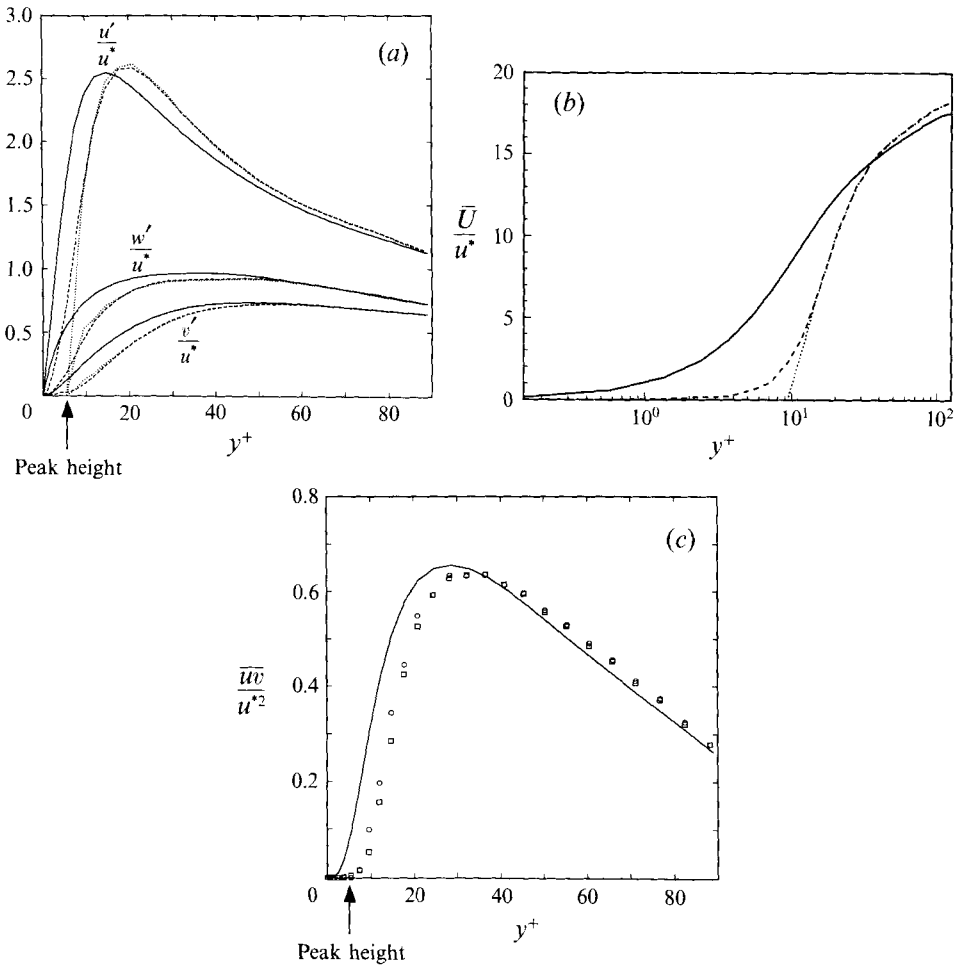

FIGURE 15. Profiles near riblets. (*a*) Fluctuating velocity profiles and (*b*) mean velocity profile: ——, Handler *et. al.*; · · · ·, above rib peaks - - -, above riblet valleys. (*c*) Reynolds stress profiles: ——, Handler *et. al.*; ○, above rib peaks; □, above riblet valleys.

and dw'/dy are clearly similar, in the riblet valleys it appears that this is not so; both u' and w' are inflectional near the height of the rib peak and du'/dy and dw'/dy are an order of magnitude smaller, deep in the valley, compared to near a flat wall. The small differences between the root-mean-square velocity profiles over the peaks and valleys disappear for distances of about $10l^*$ above the peaks. The small Reynolds stresses in the valleys raise doubt that the counter-rotating vortex pair found by Khan (1986) is related to the drag reduction phenomenon. The present results do not show substantial vertical mixing of the valley fluid.

The spanwise covariance $R_{uu}(\Delta z)$ is shown at at different heights above both the ribbed (figure 17*a*) and opposing flat wall (figure 17*b*). The streak spacing obtained from the spanwise covariance (equation (8)) near both walls is about the same, 112 for the ribbed side and 100 for the smooth side.† Even though there is a 12% difference in streak spacing, no significance is attached to this since even with a larger drag

† Henceforth, the spacing between streaks is considered to be that measured on the y-plane where the covariance minimum reaches its lowest value.

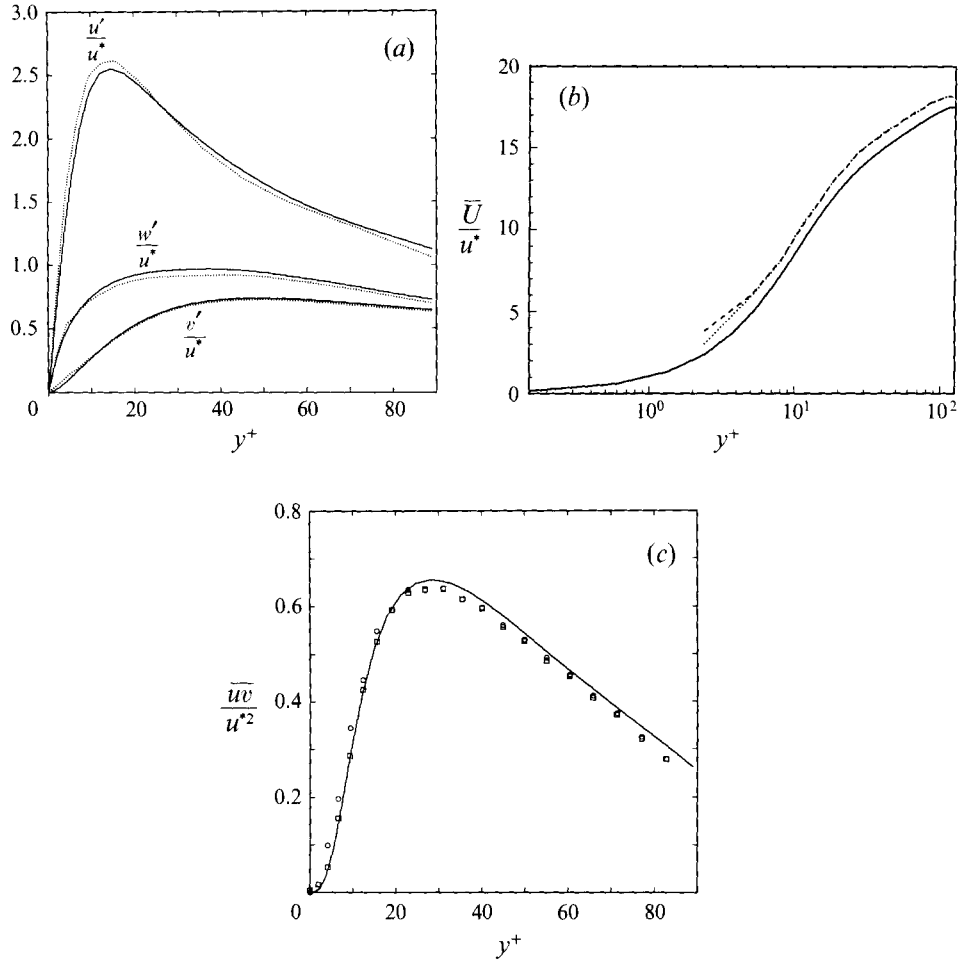

FIGURE 16. As figure 15 but offset down by the height of a riblet peak.

reduction (see Case 2 below) the streak spacing is essentially unaffected. The height of the streaks above the wall is significant, however. Over the ribbed wall the covariance minimum occurs at about $y^+ = 18$ whereas over the flat wall the minimum occurs much lower at about $y^+ = 12$. Hence, the riblets push the streaks away from the wall by an amount about equal to the height of the riblets themselves. Streak height values are estimated to be accurate to about $\pm 3l^*$.

For this riblet configuration, experiments (Walsh, 1990) indicate only a small 1–5% drag reduction. Our simulation yielded a 2.2 $\pm$1.9% decrease in drag where the error bars indicate a 90% confidence interval assuming a normal distribution for the independent realizations discussed above. With such a small drag change, the correspondingly small changes in the flow not immediately adjacent to the surface seem reasonable.

4.1.2. *Case 2 ($S^+ = 11.7$, $H^+ = 9.4$)*

The most significant drag reductions (3–8%) achieved in experiments with cusped or triangular cross-section riblets occur for $S^+ = 12$ to 15. To investigate this regime a simulation with more closely spaced riblets having $S^+ = 11.7$ and $H^+ = 9.4$ was performed (run 35). For this case it was necessary to use greater spanwise resolution,

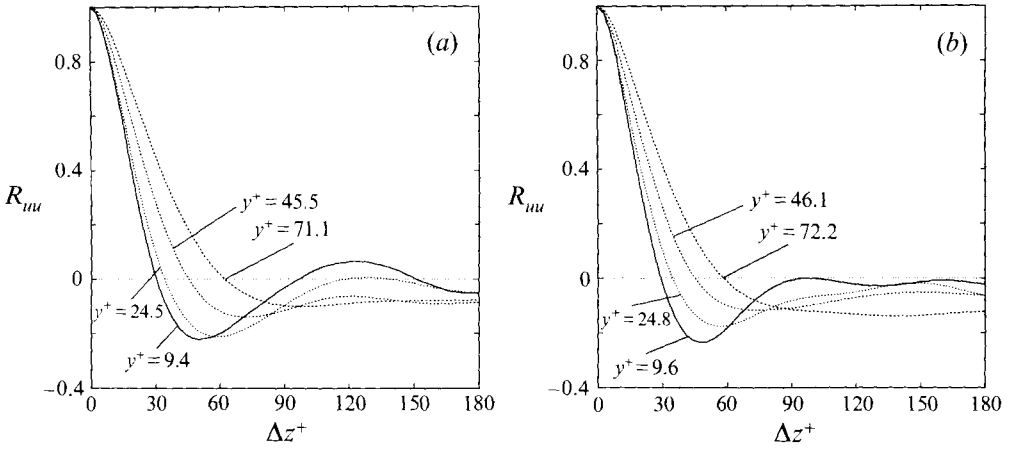

FIGURE 17. $R_{uu}(\Delta z)$ covariance at four different distances from the wall. (*a*) Near the riblet side. (*b*) Near the smooth side.

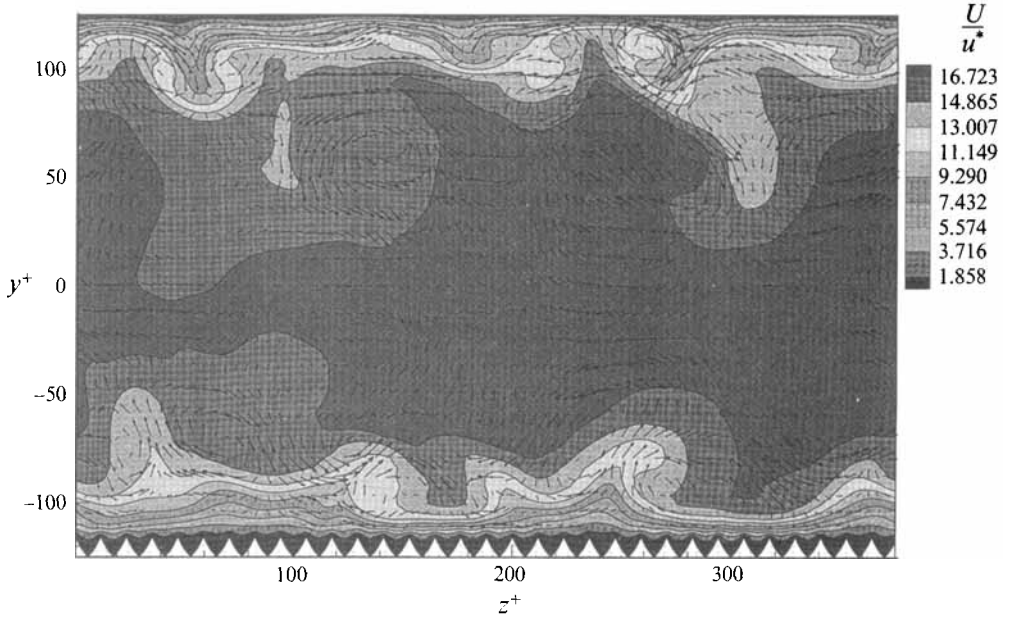

FIGURE 18. View looking down the channel in the x-direction showing contours of constant streamwise (U) velocity and selected V, W velocity vectors. Top boundary is smooth no-slip; bottom boundary has Case 2 riblets.

256 modes, to adequately resolve the ribs. The y-locations, measured in grid sites on the expanded 3/2 grid, where the velocity is brought to rest are, at successive z-locations, ... 2 4 5 6 7 8 9 8 7 6 5 4 2... The peak-to-peak spacing of the ribs is 12 expanded-grid sites and the ribs are 8 regular grid sites high. For this case there are 32 riblets along the channel width. The greater spanwise resolution in this case required a reduction in time step ($\Delta t u^{*2}/\nu = 0.078$) to satisfy numerical stability restrictions. For this geometry a drag reduction of 3.3 $\pm$2.3% was obtained using 17 independent flow realizations. This is again within the low end of the range found in experiments possibly owing to a low channel Reynolds number effect (Bruse *et al.*).

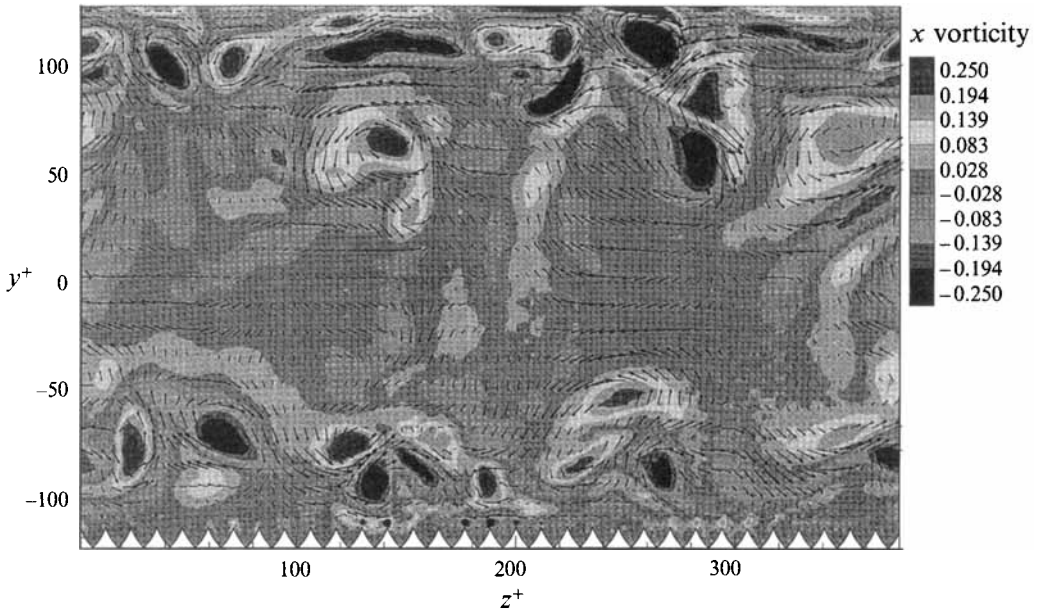

FIGURE 19. View looking down the channel in the x-direction showing contours of constant streamwise (x) vorticity and selected V, W velocity vectors.

Consider some observations based on flow visualization. Contours of constant streamwise velocity (figure 18) show, as in Case 1, that the greatest shear stress occurs immediately above the peaks as indicated by the smaller spacing of the contours there compared to the valleys. The V and W velocities deep in the valleys are very small. In animations small recirculation regions are observed in the valleys when there is a strong cross flow just above the riblet crests. A contour plot of x-vorticity (figure 19) does not, however, show much vorticity in the valleys but does show vorticity to be concentrated near crests. In an (x, z)-plane located at $y^+ = 18$ above the riblet valleys low-speed boundary layer streaks (figure 20) are clearly evident. Contours of constant wall-normal (V) velocity clearly show spanwise discreteness associated with riblet crest spacing. In animations stagnation streamlines (actually stream surfaces emanating from or re-attaching to the surface) seen in the (y, z)-plane often appear to be pinned at the riblet peaks and to jump between peaks abruptly.

The turbulence statistics near the ribbed surface are shown in figure 21(a–c) along with the same statistics adjusted for the height of the riblets in figure 22(a–c). The profiles display the same features observed with the smaller riblets except for the obvious reduction in run 34 in the maximum values of Reynolds shear stress, v', and w'. The u' profile is virtually the same as for the flat wall case and is in agreement with the smaller riblet results. These results are generally consistent with those summarized by Walsh (1990), although the present simulations indicate a clear reduction in vertical and spanwise velocity fluctuations.

Note that the Reynolds shear stress in the valleys is very small compared to the region just above the rib crest plane indicating the lack of penetration of high-speed fluid from the outer flow into the valleys. This is completely consistent with the experiments of Bacher & Smith (1985) who found that the residence time of dye in riblet valleys was much longer than near a fixed point over a smooth plate, and the transverse spreading rate of dye over a ribbed surface was less than that over a smooth surface. There is no significant difference between the location of the

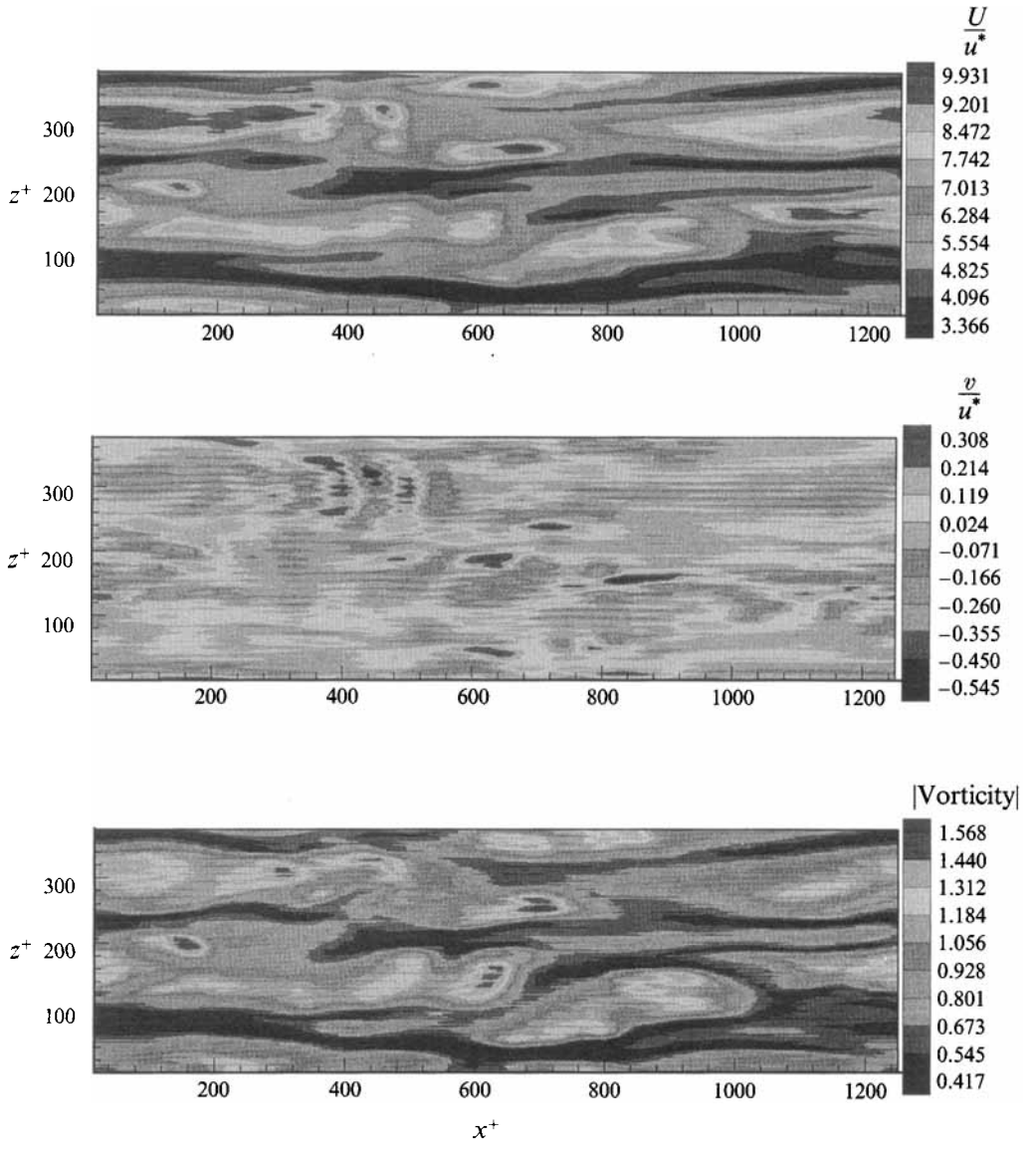

FIGURE 20. Contour plots of an (x,z)-plane at $y^+ = 18$ above the riblet valleys. (*a*) Streamwise velocity, U/u^*, (*b*) wall normal velocity, v/u^*, and (*c*) magnitude of vorticity, $|\boldsymbol{\Omega}|\nu/u^{*2}$.

maximum values of u', v' and w' over the peaks and valleys in either Case 1 or Case 2. This contradicts the results summarized in the paper by Coustols & Savill (1992) but is consistent with the idea that riblets produce mostly a local effect. The streak spacing in Case 2 is, in correspondence with the Case 1 riblet results, about the same ($104l^*$) for the ribbed as for the opposing flat wall (figure 23*a*,*b*). However, over the smooth wall R_{uu} again reaches its minimum at roughly $y^+ = 12$ while over the ribbed wall the minimum occurs higher at about $y^+ = 24$.

Small reverse-flow regions in the rib valleys are occasionally observed for the Case 2 riblets though none were observed for the Case 1 riblets. Reversed flow probably has little effect on the overall performance of the riblets but is an indicator of flow just

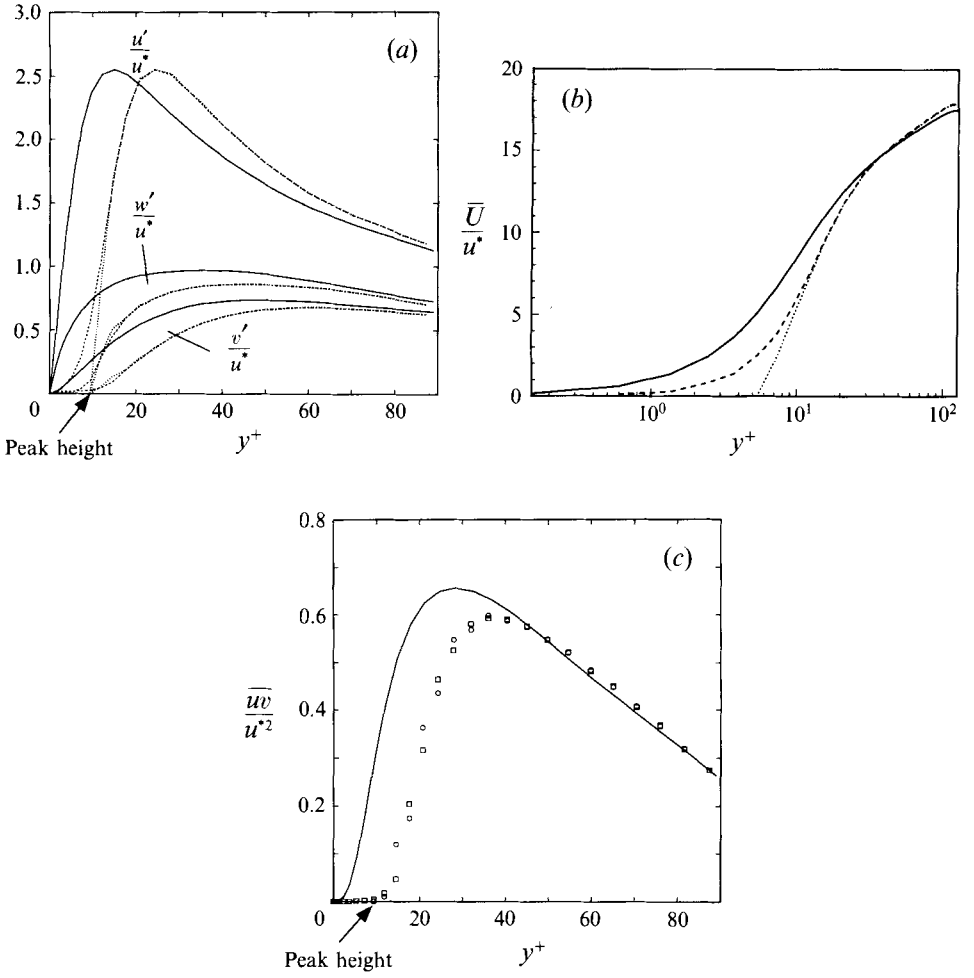

FIGURE 21. Profiles near riblets. (*a*) Fluctuating velocity profiles and (*b*) mean velocity profile: ——, Handler *et. al.*; · · · ·, above rib peaks; - - -, above riblet valleys. (*c*) Reynolds stress profiles: ——, Handler *et. al.*; ○, above rib peaks; □, above riblet valleys.

above the ribs. Chu & Karniadakis (1993) have more frequently observed reversed flow in their calculations, which may simply reflect the different riblet geometries used.

The largest velocity observed on one of the frozen grid points (x_s) was three orders of magnitude less than the channel centreline velocity, thus indicating that the force field is reacting quickly enough to track the changing turbulence and to maintain no slip.

4.2. *A possible drag reduction mechanism*

The simulations suggest possible drag reduction mechanisms due to riblets. There are several available models, each of which appears to explain some aspects of the drag reduction phenomena. Present results, in agreement with much of the work cited above, show that in riblet valleys the streamwise shear, $\mathrm{d}\overline{U}/\mathrm{d}n$, is small ($n$ is the surface normal coordinate). It therefore follows that the drag is low there. The converse is true for the rib peaks which project into the higher speed flow (see figure 11*b*). In laminar flow the reduction of drag in the valleys does not, in net, cancel the increase at the peaks. The same geometry which gives rise to

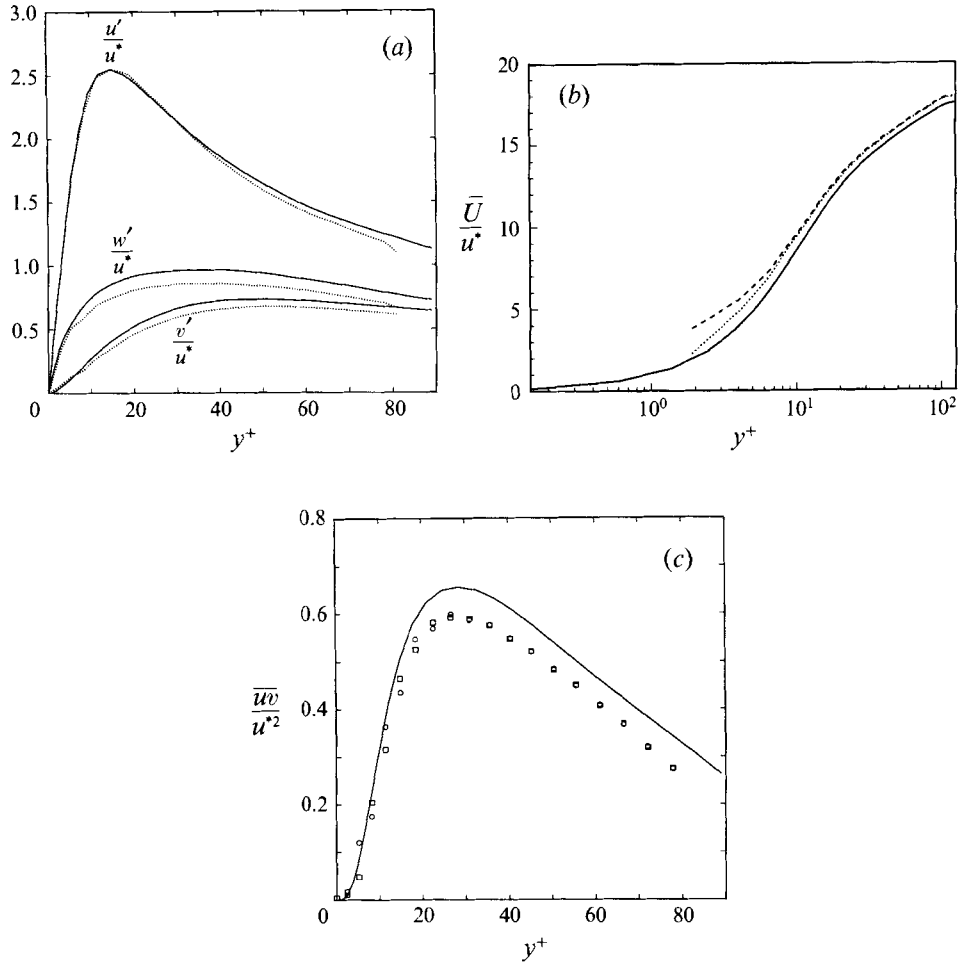

FIGURE 22. As figure 21 but offset down by the height of a riblet peak.

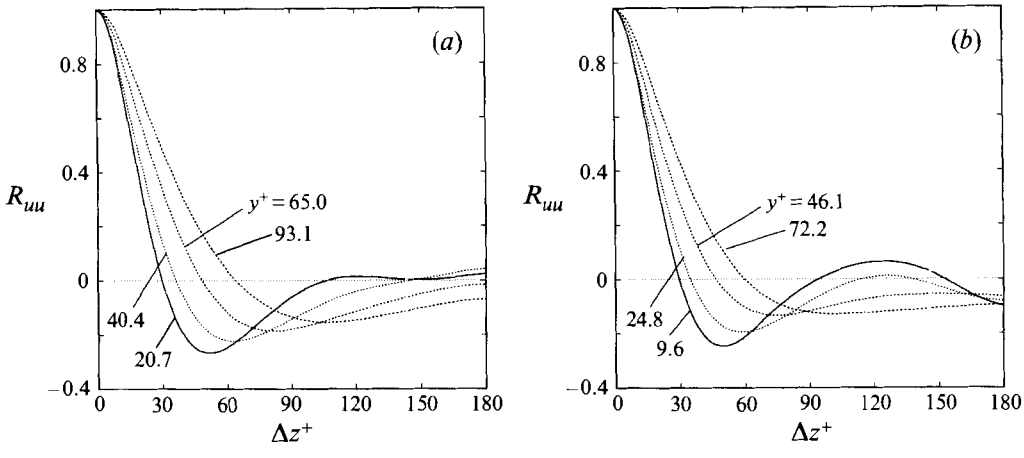

FIGURE 23. $R_{uu}(\Delta z)$ covariance at four different distances from the wall. (*a*) Near the riblet side. (*b*) Near the smooth side.

a drag increase in laminar flow gives, somewhat paradoxically, a drag decrease in turbulent flow. Riblets possibly restrict development of streamwise low speed streaks due to streamwise vortices. Yet the optimum peak-to-peak riblet spacing is only about a third to a half of a typical quasi-streamwise vortex diameter ($\approx$ 30–40l^*, Wallace & Balint 1988), not nearly wide enough to surround a streak or a vortex. Also, the present results do not show a substantial change in spanwise streak spacing over a ribbed surface compared to the flat-plate case.† Animations of the simulations do not exhibit the typical quasi-streamwise vortices settling between smaller riblets although small vortices (figure 11*b*) have been observed to live for some period of time in the valleys. However, one effect that is evident in animations is that the spanwise meandering of the streaks, which is noticeable in flat-plate flows, appears to be damped over the riblets. In addition, and perhaps for the same reason, separation or re-attachment events are evident primarily on rib crests.

In the two simulations of turbulent flow over riblets discussed herein, it was found that the minimum in R_{uu} is displaced away from the wall by a bit more than the riblet height (Bechert & Bartenwerfer 1989 and Choi *et al.* 1991*b* also note the displacement of the streaks). Yet from these observations it is not clear whether the displacement of the streaks is a cause or an effect of the drag reduction. Perhaps if the vortices are further away they pump less high-speed fluid toward the wall and hence the drag is reduced. Another possibility is that since the riblets reduce drag, the region of highest shear moves away from the wall, and, considering the results of Lee, Kim & Moin (1990) which show that streaky structures can be due principally to the action of the mean shear, the streak displacement may be an effect of the drag reduction.

Riblets might also be thought to damp wall normal fluctuations by deflecting upward a downward burst of fluid, thereby countering its effect and perhaps pushing the associated vortical structures away from the wall. This is, in a sense, a passive mechanism analogous to a smart surface that performs wall normal blowing and sucking to reduce turbulent fluctuations. As a boundary layer vortex approaches a rib, the rib peak sheds vorticity of opposite sign. This is like the observed behaviour near a flat surface except that the shed vorticity from the rib peak is more concentrated. Perhaps the concentrated regions of vorticity observed by Choi *et al.* (1991*b*) and in the current simulations near rib peaks suffer more intense dissipation than do the more diffuse patches of vorticity which occur near flat walls. In this sense, the turbulence may be more strongly dissipated near riblets.

Walsh (1990) suggests and the above discussion indicates (also see Bacher & Smith 1985; Bechert *et al.* 1986; Bechert & Bartenwerfer 1989, Coustols & Savill 1992; Luchini, Manzo & Pozzi 1991) that riblets work by effectively providing an enhanced cross-stream resistance to the vortical near-wall motion near the riblet crests. The idea is intuitively appealing but to this point it is only a conjecture. Suppose, however, that one wishes to isolate the effect of the damping of the spanwise velocity fluctuations near the riblet peaks from the other effects of riblets. The strong nonlinearity of the flow does not permit a simple superposition of the individual isolated effects of riblets. Yet a careful choice of the effects to be isolated should elucidate some of the important mechanisms underlying riblet drag reduction as we show next.

† Others have found differences. See Walsh (1990) for riblet results and Handler *et al.* (1993) for a discussion of polymer additive results.

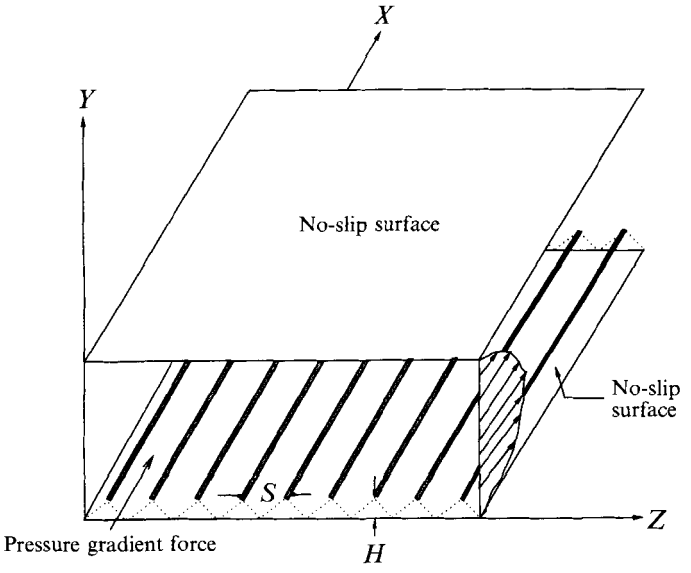

FIGURE 24. Geometry for flow simulation of channel bounded by two impermeable no-slip boundaries and containing lines (grey) along which the w velocity is damped. These schematically drawn lines of force represent the effects of the crests of the riblets. A uniform pressure gradient force is applied throughout the domain.

4.3. *Simulation of modelled riblets*

4.3.1. *Wire-like region of cross-flow damping*

To determine the effect of cross-flow damping, simulations were performed in which a damping of the spanwise (w) velocity fluctuations is imposed on the flow at locations which are representative of real rib crests. The geometry for the modelled flow is given in figure 24. Such damping is easily applied by creating a force field only in the z-direction with $\alpha = 0$ and choosing a damping constant, β (see (3)). In this way, there is no net force applied to the flow in any direction. The spacing between rib peaks, the height of the peaks and the magnitude of damping β are all varied thereby exploring a region of the parameter space governing the flow physics. The force field corresponds to part of the effect which would be created if a fine wire had replaced each riblet crest. For these simulations (runs 36–52) the computational domain is 1250, 250, and 625 viscous units in the x-, y-, and z-directions respectively and the boundary condition on the surface below the force field is $\boldsymbol{U} = 0$ (no slip). Details of additional computational parameters for each run are given in table 4. For each run 32 independent realizations were obtained.

The turbulence statistics for representative run 36 ($S^+ = 18.4$, $H^+ = 5.1$, and $\beta = 5$), which has roughly the same dimensions as the full riblet simulation (Case 1), are shown in figure 25(a–c). The asymmetry of the profiles clearly indicates that the spanwise damping near one wall is having a strong effect on the turbulence. For clarity, the velocities were normalized by a unit velocity as opposed to the local friction velocity, so as to accentuate the asymmetry. There is a drag decrease on the damped side of the channel and a resulting overall mass flux increase. The Reynolds shear stress and fluctuating velocities near the damped wall are noticeably decreased compared to the undamped side. The turbulence profiles above the damped wall have also been normalized by the damped wall friction velocity and length scale in figure 26(a–c). The resultant profiles show much the same trends as the statistics from the

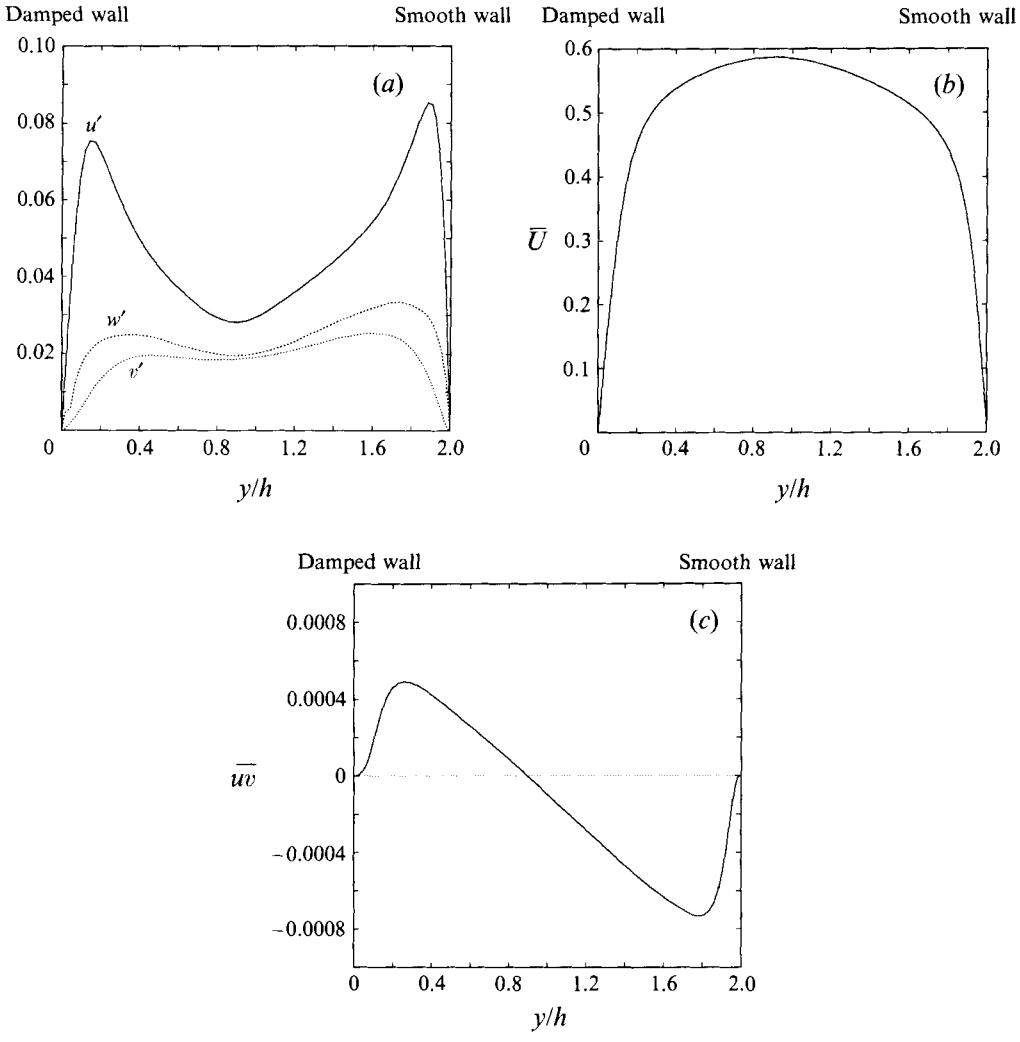

FIGURE 25. (*a*) Fluctuating velocities across the whole channel. (*b*) Mean velocity profile. (*c*) Reynolds shear stress. No normalization is used so the two sides may be compared. Note the asymmetries.

full riblet simulations. The Reynolds shear stress and v' and w' peak amplitudes are reduced and the peaks are shifted further from the wall while the u' peak is shifted away from the wall. There is little difference between the u' and v' over the damped rib crests (that is, the wire-like structures) and over the valleys (the regions midway between the crests corresponding to the real riblet valleys). Near the crest plane ($H^+ \approx 5$) there is a sizable decrease in w' over the valleys and a much larger dip right at the peak. This difference between the crest and the valley does not propagate far into the flow. There also is a small increase in $\overline{uv}$ immediately above the crests compared to that over the valleys, which we did not observe over the fully modelled riblets. The mean velocity profile exhibits a linear sub-layer and a clear log-layer with an apparent increase in the vertical extent of the buffer zone, an effect also seen in the riblet simulations.

The streak spacing near the damped wall (λ^+), as for the riblet wall, is about 110

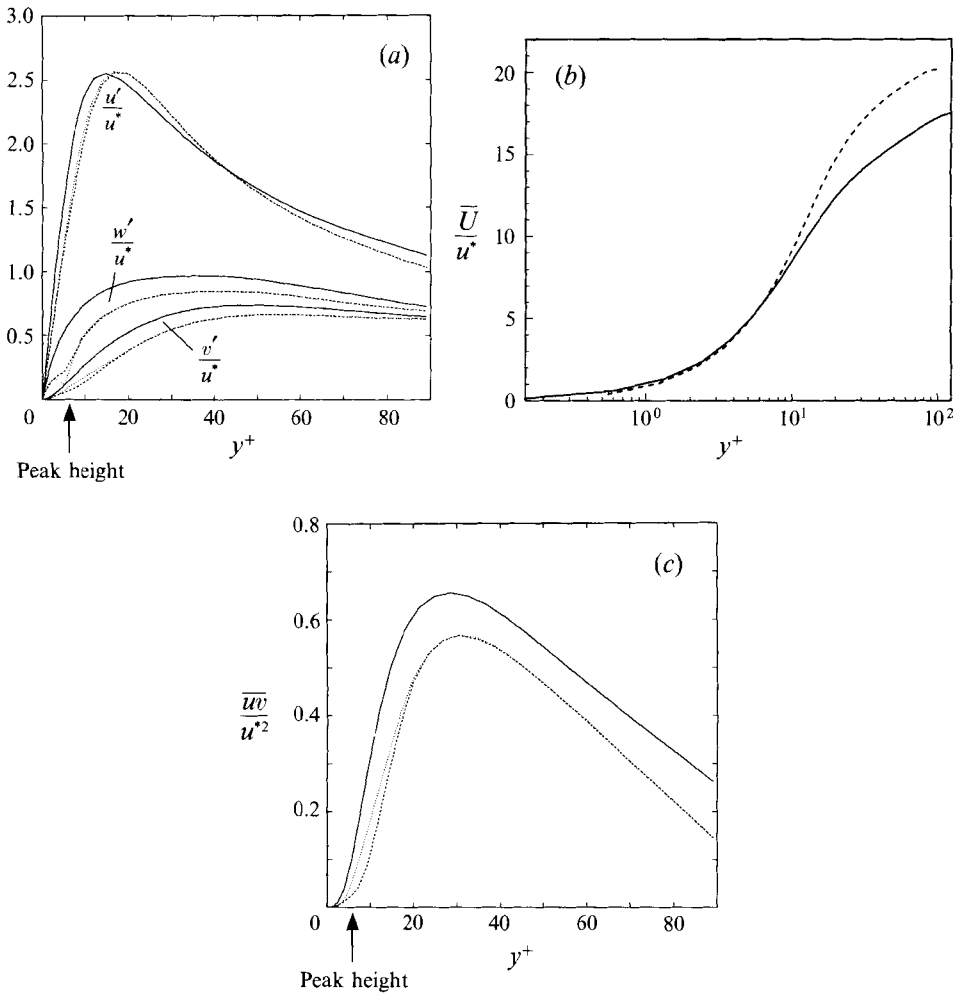

FIGURE 26. Profiles near w-damped wall. (a) Fluctuating velocity profiles, (b) mean velocity profile and (c) Reynolds shear stress profiles: ——, Handler *et. al.*; · · ·, above crests; - - -, above valleys. In (b) the dashed line denotes above both crests and valleys.

(figure 27). The covariance R_{uu} reaches its minimum at about $y^+ = 19.8$, about 8 wall units farther from the wall than for a flat surface. The dependence of the height of the streaks above the wall on wire spacing, (H^+ held constant) is shown in figure 28. As S^+ drops to less than about 30, the streaks rise above the plane on which the spanwise damping is applied. This is consistent with the observation by Coustols & Savill (1992) that blade-like riblets with $S^+ < 35$ displace eddies away from the wall while more widely spaced riblets do not have this effect. If the average streak spacing is about 100, the vortex core spacing should be about 50 so that for S^+ larger than 50 one expects that the vortices might settle between the crests. An S^+ of roughly 25 (half the core spacing and less than a core diameter) or less can be expected to keep the vortices away from the wall. This conjecture is confirmed by the results shown in figure 28 and is consistent with the results from the full riblet simulations. This is also consistent with the experimental finding that drag reducing ribs must be spaced less than about $30l^*$ apart to be effective in reducing drag. In general, the present results show no trend in the variation of the streak spacing with S^+ (or for that matter, H^+

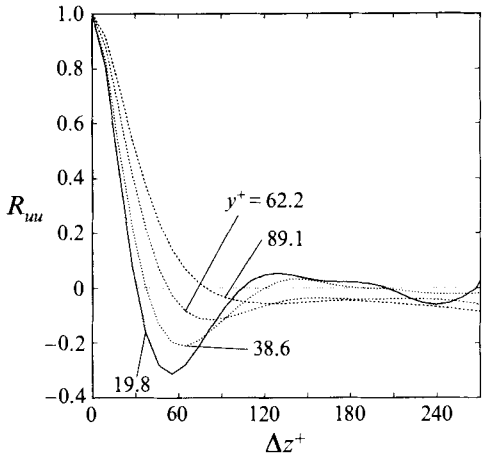

FIGURE 27. $R_{uu}(\Delta z)$ autocorrelation at four different distances from the wall near the damped side.

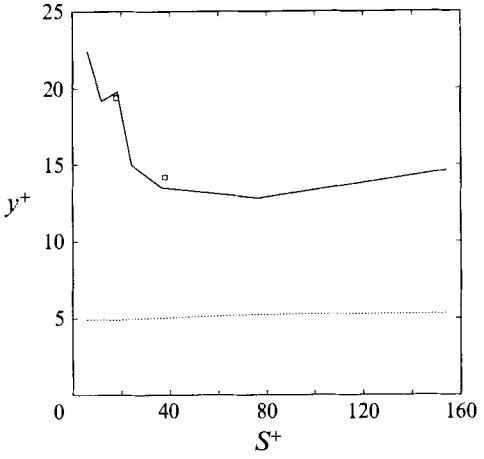

FIGURE 28. Streak height above the boundary (defined as height of absolute minimum in R_{uu}) as crest spacing is varied. ——, Wire-like model; □, fence-like model; · · · ·, height of crests (shown for reference).

and β); the streaks tend to retain their 105 ± 15 spacing. Finally, note that reverse flow ($u < 0$) commonly occurs right near the wall below the spanwise damping field. This is probably because the boundary layer has been slowed and thickened and the flow is thus more easily separated by an external pressure fluctuation.

The effect of spanwise damping on surface drag is now considered. In figure 29(*a*) the dependence of the drag ratio on S^+ ($H^+ \approx 5$ and $\beta = 5$) is shown. It is evident that the more closely spaced the rib peaks the lower the drag and the greatest drag reduction (29%) occurs for $S^+ = 5.8$. When S^+ drops below about 11, however, the drag reduction saturates. These results are intriguing in light of the experimental data for riblets compiled by Walsh (1990) in which there is a drag reduction maximum for $S^+ \approx 12$. The large drag reductions compared to those of real riblets occur mostly because real riblets project substantial wetted surface area into the high-speed flow away from the wall whereas the damping field does not. For large S^+ there was little drag reduction. However, unlike in the riblet experiments, spanwise damping never

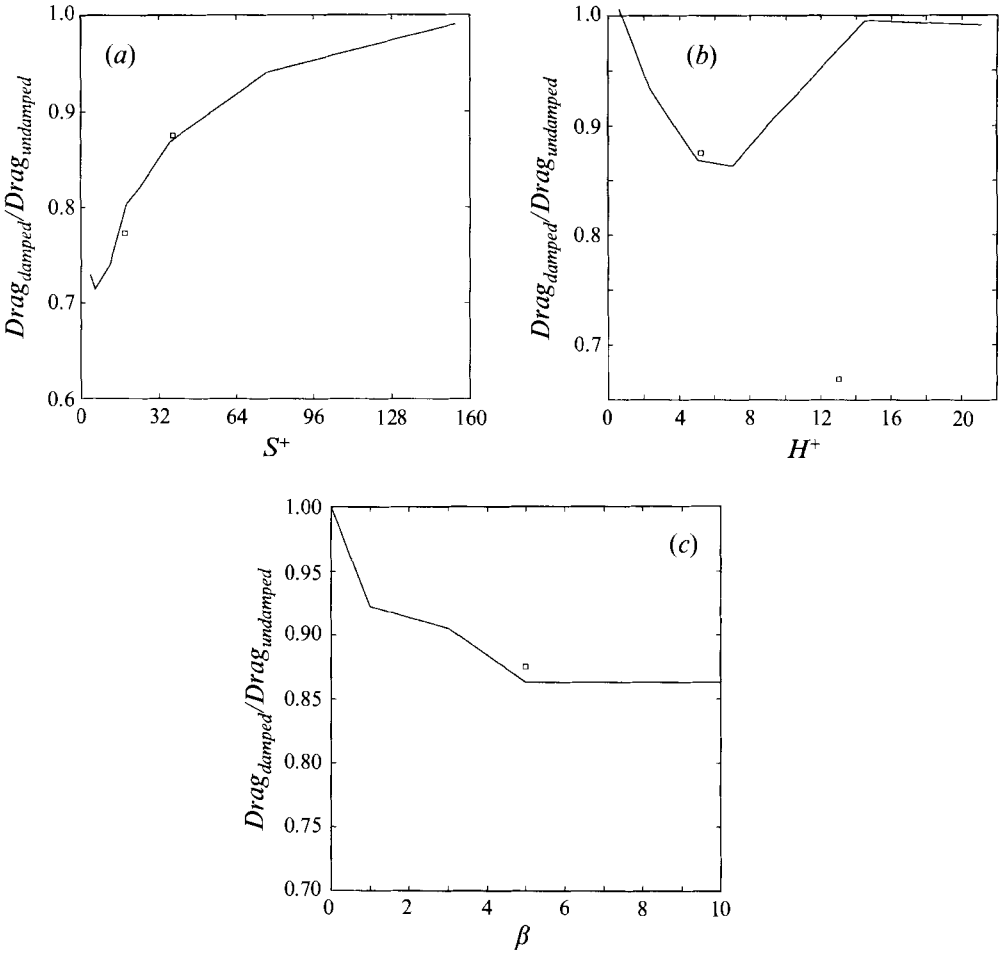

FIGURE 29. Drag ratio of bottom boundary to top boundary as (*a*) the spacing between crests is varied, $\beta = 5$ and $H^+ \approx 5$; (*b*) H^+ varies for a fixed crest spacing ($S^+ \approx 36$) and damping constant ($\beta = 5$); (*c*) β is varied for a fixed crest spacing ($S^+ \approx 36$) and height ($H^+ = 5.3$). ——, Wire-like model; □, fence-like model.

appears to increase drag for any value of S^+, indicating that cross-flow damping is only a beneficial effect.

In figure 29(*b*) the dependence of the drag ratio on H^+ ($S^+ \approx 37$ and $\beta = 5$) is shown. There appears to exist an optimal value of H^+ (≈ 7) which gives the lowest drag. For smaller H^+ the local w-fluctuations are already small so the damping has little effect. For larger H^+ it appears that the flow below H^+ recovers from the damping sufficiently so that there is little effect on the turbulence except for the w' profile, which still shows a localized dip (figure 30). These results at first appear to indicate that there is an optimal rib height similar to that found in the results compiled by Walsh (1990) of between $5l^*$ and $15l^*$. However, the presence of cross flow below the damping wires does not correspond to what can occur below a solid riblet's crest where obviously no fluid may flow. This difficulty is discussed further in §4.3.2.

Finally, consider the effect of varying the strength of the damping parameter. If one assumes that very rounded riblets (virtually a flat wall) have little damping effect and that sharply peaked ribs probably have the greatest effect (see Bechert *et al.*

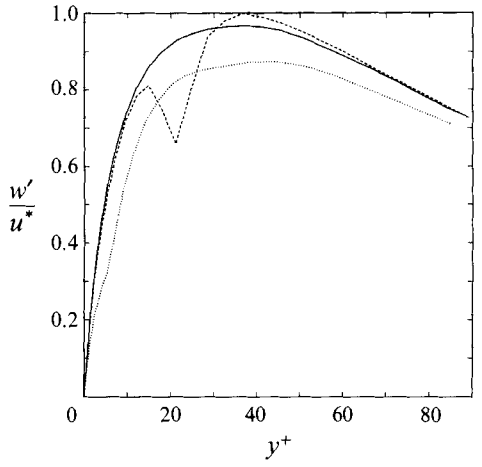

FIGURE 30. Spanwise averaged w' profiles normalized by u^*_{damped}. ——, Handler *et al.*; - - -, $H^+ = 21.1$, $\beta = 5$, $S^+ = 36.6$; · · · ·, $H^+ = 5.3$, $\beta = 5$, $S^+ = 36.6$. Note how, for the $H^+ = 21.1$ case, the fluctuations recover below H^+.

1986; Chu & Karniadakis 1993; Luchini *et al.* 1991; Walsh 1990) one can investigate the effect of sharpness by varying β. The connection between β and the sharpness of a real riblet peak is tenuous and simply reflects the assumption that a sharp peak will resist cross-flow more effectively than a smooth peak and that β is a qualitative measure of the resistance. The effects of varying the damping ($H^+ = 5$ and $S^+ = 36$) on drag are shown in figure 29(*c*). Drag benefits from increasing β appear to saturate at some point and drag is not further reduced by increasing β further. This saturation may have implications for the usefulness of trying to sharpen experimental riblets.

4.3.2. *Fence-like region of cross-flow damping*

The wire-like cross-flow damping model neglects the effects of no cross-flow which occurs below real riblet peaks. To model this effect, additional simulations were performed in which the cross flow damping was applied on rib peaks as well as on all grid sites directly below the peaks. This situation is analogous to modelling small boundary layer 'fences' which do not directly affect the wall normal and streamwise velocities. The drag results obtained with these fence-like configurations are given in figure 29 (runs 53–56; table 4). It is found that the fence- and wire-like models correspond well unless H^+ is large. For large H^+ fluid can flow under the wires but not under the fences and the drag reducing effect of the fences increases with increasing H^+. If the wires are close to the wall, little of the viscous cross-flow can pass between the wires and the wall through the narrow gap. Thus, the optimal H^+ value discussed in the previous section and seen in figure 29(*b*) for wire-like structures is not expected to apply to real riblets which prevent all flow below the peaks.

For fences (or wires) which are closely spaced, u' over the peaks and valleys is nearly the same, but for fences, if S^+ is increased, u' and the Reynolds shear stress over the peaks becomes appreciably greater than the corresponding values over the valleys (see figure 31*a–c*). This qualitative observation is in agreement with the recent experimental results of Vukoslavcevic *et al.* (1992) in which, for riblets with $S^+ = 35$ and $H^+ = 17.5$, u' is found to be 12% greater over the peaks than over the valleys. The present results show a similar but less obvious separation between the peak and valley curves of v' and w'. It appears that widely spaced riblets, fences, or wires deflect

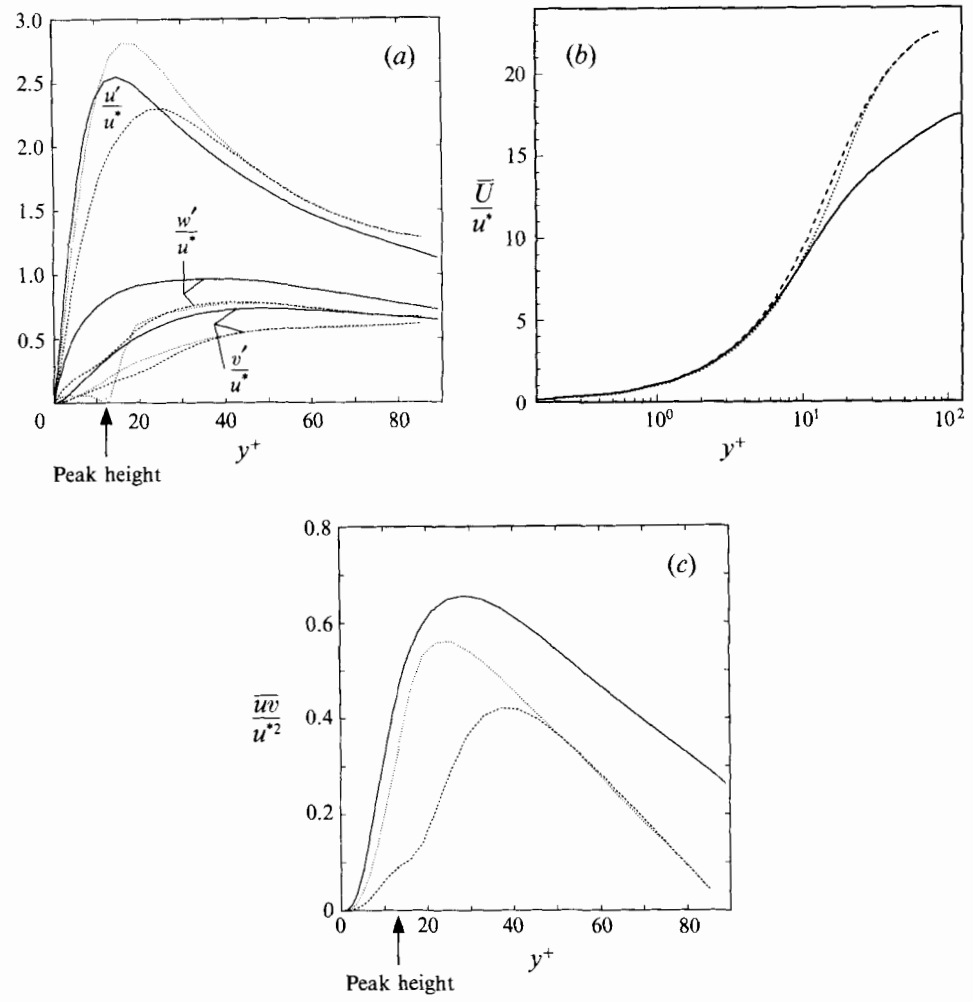

FIGURE 31. Profiles near w-damping fences. $H^+ = 13$, $\beta = 5$, $S^+ = 34.5$. (*a*) Fluctuating velocity profiles, (*b*) mean velocity profile and (*c*) Reynolds shear stress profiles: ——, Handler *et al.*; - - -, above valleys; · · · ·, above crests.

the cross-flow up and over the peaks and that this brings high-speed fluid toward the wall and low-speed fluid away from it; hence, u' and the Reynolds shear stress is locally enhanced. If the wires or fences are closely spaced there is little cross-flow motion in the valleys to be deflected. This suggestion differs from the explanation by Vukoslavcevic *et al.*, that the riblet is inclined away from the peak and is thus less effective in damping u' fluctuations; w' damping fences or wires cause the same effect without directly damping u' at all. Note that for the fences $\beta = 5$ so the damping is strong enough to nearly halt the cross-flow.

4.3.3. *Real wires over a flat plate: Kramer's idea*

For a comparison with the riblet, wire-like damping and fence-like damping simulations, consider one final calculation in which a set of real wires is modelled. This is essentially the situation described by the Kramer patent (1937). All three velocity components are brought to zero on a string of grid points at $S^+ = 40.5$ and $H^+ = 5.5$

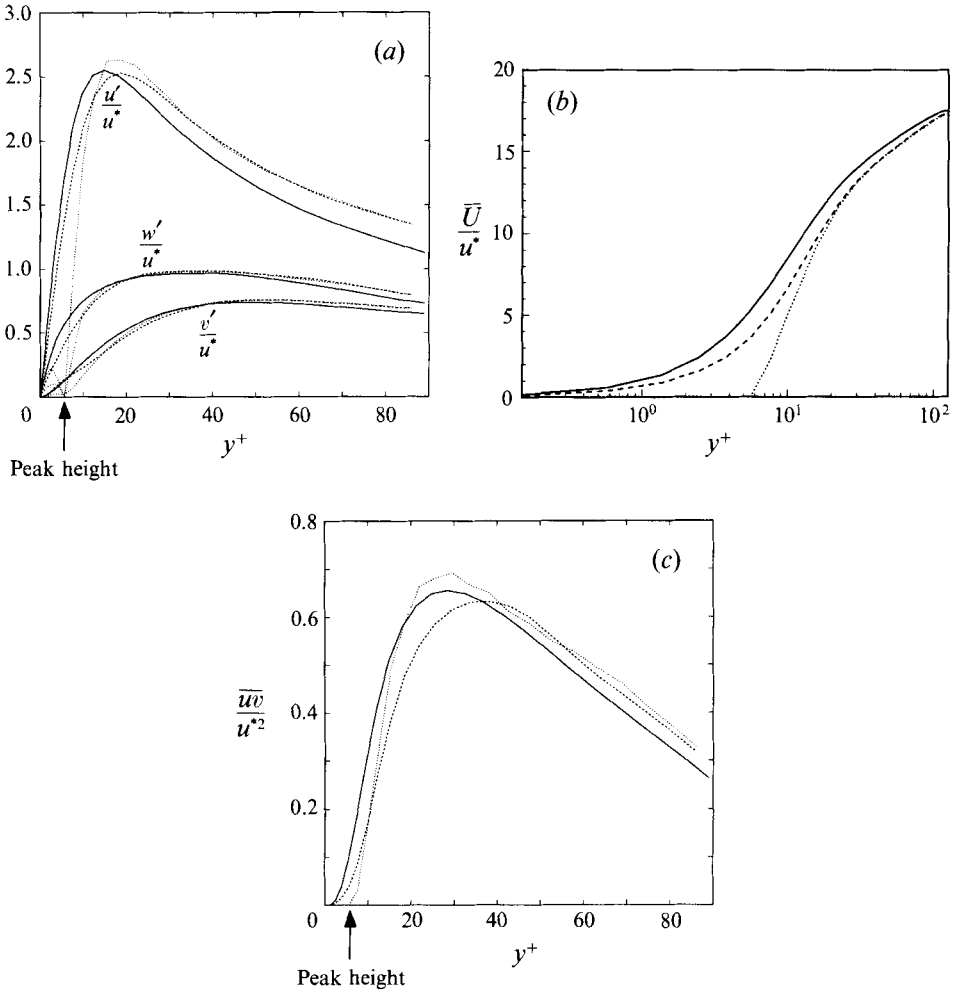

FIGURE 32. Profiles near modelled wires. $H^+ = 5.6$, $S^+ = 40.5$. (*a*) Fluctuating velocity profiles, (*b*) mean velocity profile and (*c*) Reynolds shear stress profiles: ——, Handler *et al.*; - - -, above valleys · · ·, above crests.

in effect representing fine, unresolved wires at these locations. As discussed earlier, if only w-fluctuations are damped there is a 16% drag reduction on the damped side of the channel underlying the damping region. With the real wires, however, the net drag is found to increase by 5%. This result is in modest agreement with the results of Bruse *et al.* On the real wires, of course, there is streamwise drag whereas on the w-damped 'wires' there was none. In figure 32(*a–c*) the mean profiles from this run are shown. The values of u^* and l^* used here are those found by assuming that the shear stress is the total shear stress which is the sum of that on the wall and the wires. The u' maximum is displaced away from the wall and is greater over the wires than between them, and v' and w' are little affected except near the wires. The maximum Reynolds shear stress is 12% greater over the wires than over the valleys. These effects are very much like those described above (§4.3.2) and indicate that widely spaced real wires also deflect cross-flow up and down. The mean streamwise velocity profile has been shifted down and to the right as would happen over three-dimensional surface roughness. Below $y^+ = 15$ R_{uu} (not shown) has very strong correlations at a spacing

of $40.5l^*$ corresponding to the viscous effect of evenly spaced protrusions into the flow. Above $y^+ = 15$ the correlation returns to that found over a flat plate with a streak spacing of about $102l^*$. A range of wire heights and spacings must be tried before further conclusions can be drawn.

5. Summary and discussion

5.1. *Numerical approach*

The method of virtual boundaries has enabled the modelling of a relatively complex boundary geometry by means of a spectral code. Simulations of laminar flow over riblets were used to explore the sensitivity of the solutions to grid resolution, smoothing techniques, and certain boundary conditions. A detailed analysis of turbulent flow over a virtual flat plate was performed. These and other tests strongly support the correctness of our simulations.

The simulation of riblets with body forces appears unique in that a spectral code already validated for turbulent channel flow in can easily be modified to approximate a complex geometric structure on one of the boundaries. While the method of virtual boundaries is not an exact simulation of solid boundaries, it is a quantitatively accurate model calculation for the geometries in which it has been tested. Although the method has several drawbacks, these can be largely overcome by the methods discussed earlier, and it appears that the technique may be useful for obtaining a reasonably accurate representation of a surface. As with any other computational technique where surface details are of interest, it is necessary to have a non-uniform mesh that concentrates grid points near the surface. For example, in the riblet calculations of Choi *et al.* (1991*a*,*b*), Chu *et al.* (1992) and Chu & Karniadakis (1993) mesh points could be concentrated right along the rib surface. In the present calculations the Chebyshev cosine grid did enable us to concentrate grid points near the riblets, though not in an optimal way. The fact, however, that the spanwise grid spacing was everywhere constant (128 or 256 modes in the full riblet computations) was costly in that the increased z-resolution was not needed away from the ribbed surface.

5.2. *Simulations over riblets and modelled riblets*

The virtual surface approach was used to simulate fully turbulent flow over small and large riblets. The mean and fluctuating velocity and Reynolds shear stress profiles for both cases were compared with those over a flat plate. Two-point autocorrelations of the streamwise velocity were used to determine the characteristics of the low-speed boundary layer streaks. Based on these results, a simple model for the beneficial effect of riblets on turbulent flow was described. The hypothesis is that riblets reduce drag in part because of the damping of spanwise velocity fluctuations by the rib crests. To test this idea, simulations were performed in which the force field was used to damp only the cross-flow.

While most of the present results for full riblet simulations correspond well with those of Chu & Karniadakis (1993), one does not: the present results do not show the small hump they find in the u' and w' profiles in the riblet valleys. This difference may be due to the greater sharpness of their riblet peaks which allowed the ribs to more easily shed vortices which can then form recirculation cells in the valleys. It is interesting to note, however, that the experiments of Vukoslavcevic *et al.* (1992) on $H^+ = 17.5$ and $S^+ = 35$ ribs show no hump. Hence, the presence and or importance of the hump remains an open question.

It appears that the model of riblet peaks providing a damping of the spanwise velocity fluctuations may explain many of the effects caused by real riblets. Depending on the parameters, there can be large drag reductions on the surfaces above which spanwise damping was used. The turbulence statistics and the dependence of drag on (modelled) riblet height and spacing were found to be remarkably similar to the results obtained with full riblets. We believe that we have demonstrated for the first time that cross-flow damping alone can explain many of the effects of riblets in turbulent flow.

These damped wire simulations may clarify a principal drag reduction mechanism proposed for riblets and help answer the question: is the upward displacement of the streamwise streaks a cause of the drag reduction or an effect of it? A real riblet presents a solid surface exposed further into the flow than does a flat plate. This displaces the region of high shear, due to the no-slip condition, away from the wall. Lee *et al.* (1990) note that streaky structures appear in sheared turbulent flow simply due to the action of the shear so that riblets might be expected to displace the streaks by changing the y^+ location of maximum shear. The w' damping calculations show, however, that even without directly acting on the U velocity component (and hence without directly affecting $\mathrm{d}\overline{U}/\mathrm{d}y$) the ribs can displace the streaks by deflecting upward the cross-flow motion caused by the vortices. The vortices themselves can then cause an increase in shear in the y^+ region where they reside (by vertical stirring) and their displacement can result in a decrease in wall shear below that region. This means that, while the presence of a no-slip surface can contribute to the displacement, it need not be the sole cause of that displacement.

Experiments related to the simulation of real wires have been performed. Johansen & Smith (1983, 1986) placed monofilament fishing line flush against a flat plate in turbulent flow and studied streak formation and certain velocity profiles. Their fishing line (diameter $= 4l^*$) was generally spaced more widely than our wires. Nonetheless, their data are remarkably similar to ours. In the data they present for u' for a case of $S^+ = 142$, $H^+ = 4.2$ (hence, widely spaced wires with a height nearly the same as ours) they too find that u' over the valleys is greater than over the peaks for $y^+ <$ about 10. This order is then switched for $10 < y^+ < 30$ and then the two profiles are about the same for $y^+ > 30$. They also find that the wires essentially displace the peak in the u' profile away from the wall by the height of the wire. They found that the streak spacing was fixed at S^+ for values of y^+ of around 10 or less but that the spacing reverted to that of a regular flat plate for y^+ of 15 and higher. They interpreted their results as the fishing line 'focusing' the streaks above the line or as acting as 'nucleation sites for streak formation'. It appears that the relative insensitivity of streak spacing (normalized by the viscous length scale) for y^+ of 10 or more wall units above the protrusions, to either their different experimental values of S^+ or our various parameters discussed above, indicates that the streaks can be displaced upwards but that their spacing is set by the mean wall shear stress. The viscous 'focusing' effect remains within the viscous sublayer.

For a physical experiment it is difficult to conceive of a way to non-intrusively damp one velocity component in non-conducting fluids. Experiments in conducting fluids, where a strong magnetic field is applied to damp fluctuations in pipe/duct flow, do show large drag reductions (Tsinober 1990). In those flows uni-directional damping makes the flow (locally) more two-dimensional with a resulting inverse energy cascade (small scales to large scales). The present simulations do not, however, show a clearly two-dimensional flow (mostly u' and v', with little w') in the valleys between riblets, wires or fences.

We have also briefly tried other damping schemes. Spanwise damping in the whole

volume of flow below the rib peaks ($H^+ \approx 5$) produced slightly different results from damping only at the rib peak plane for small values of S^+. Damping v instead of w did produce some drag reduction (perhaps up to 20%, depending on the configuration) but generally not as much. This is probably because near a wall v' is already quite a bit smaller than w' and there is thus little motion to damp. Choi, Moin & Kim (1991*b*) and Moin, Kim & Choi (1989) have also modelled a method of actively controlled wall normal blowing and sucking to damp v' and found a similar drag reduction. The greater effect we find, however, by damping spanwise velocity fluctuations may indicate that a spanwise component to a blowing jet may be useful.

The overall image we obtain for the effects of riblets is that their beneficial effect can be simply described as damping cross-flow fluctuations. Very short riblets do not protrude far enough into the flow to sufficiently damp w (or v) fluctuations. Larger riblets, $S^+ \approx H^+ \approx 10$ to 20 do damp w and have lower drag in the valleys but produce greater drag near the rib peaks. Ribs that are spaced closely enough do not allow the large boundary layer streamwise vortices to settle between them. The drag benefit of riblets, probably from displacing the streamwise vortices, reaches a maximum as S^+ drops below about 12. Widely spaced ribs, while still able to damp fluctuations, allow the boundary layer vortices to lie in the valleys. These vortices can bring high-speed fluid close to the wall and reduce the riblet effectiveness.

The work presented here was in part supported by a gift from ORMAT Industries and by the Fluid Dynamics Task Area of the Naval Research Laboratory. The computations were performed at the Pittsburgh Supercomputing Center and the University of Texas Center for High Performance Computing and were supported by a grant from Cray Research Inc.. Helpful conversations with L.-P. Wang are gratefully acknowledged.

REFERENCES

BACHER, E. V. & SMITH, C. R. 1985 A combined visualization-anemometry study of the turbulent drag reducing mechanisms of triangular micro-groove surface modifications. *AIAA Paper* 85-0548.

BECHERT, D. W. 1987 Experiments on three-dimensional riblets. Presented at *Turbulent Drag Reduction by Passive Means Conf. 15-17 Sept., London.* Royal Aeronautical Society.

BECHERT, D. W. & BARTENWERFER, M. 1989 The viscous flow on surfaces with longitudinal ribs. *J. Fluid Mech.* **206**, 105–129.

BECHERT, D. W., BARTENWERFER, M. & HOPPE, G. 1990 Turbulent drag reduction by nonplanar surfaces - a survey on the research at TU/DLR Berlin. In *Structure of Turbulence and Drag Reduction: IUTAM Symp., Zurich, 1989* (ed. A. Gyr), pp. 525–543. Springer.

BECHERT, D. W., BARTENWERFER, M., HOPPE, G. & REIF, W. E. 1986 Drag reduction mechanism derived from shark skin. *15th Congress of the Intl Council of Aeronautical Sciences, Sept. 7–12, London, UK.* ICAS-86-1.8.3.

BECHERT, D. W., HOPPE, G. & REIF, W. E. 1985 On the drag reduction of the shark skin. *AIAA Paper* 85-0546.

BERNARD, P. S., THOMAS, J. T. & HANDLER, R. A. 1993 Vortex dynamics and the production of Reynolds stress. *J. Fluid Mech.* **253**, 385–419.

BROOKE, J. W. & HANRATTY, T. J. 1993 Origin of turbulence-producing eddies in a channel flow. *Phys. Fluids* A **5**, 1011–1022.

BRUSE, M., BECHERT, D. W., HOEVEN, J. G. TH. VAN DER, HAGE, W. & HOPPE, G. 1993 Experiments with conventional and with novel adjustable drag-reducing surfaces. In *Near-Wall Turbulent Flows* (ed. R.M.C. So, C. G. Speziale & B. E. Launder), pp. 719–738. Elsevier.

CHOI, H., MOIN, P. & KIM, J. 1991*a* On the effect of riblets in fully developed laminar channel flows. *Phys. Fluids* A **3**, 1892–1896.

CHOI, H., MOIN, P. & KIM, J. 1991*b* Turbulence control in wall-bounded flows using direct numerical simulation. In *Proc. Turbulence Structure and Control, April 1–3, Columbus, OH*, pp. 68–73.

CHU, D., HENDERSON, R. & KARNIADAKIS, G. 1992 Parallel spectral-element-Fourier simulation of turbulent flow over riblet-mounted surfaces. *Theor. Comput. Fluid Dyn.* **3**, 219–229.

CHU, D. & KARNIADAKIS, G. 1993 The direct numerical simulation of laminar and turbulent flow over riblets. *J. Fluid Mech.* **250**, 1–42.

COUSTOLS, E. & SAVILL, A. M. 1992 Turbulent skin-friction drag reduction by active and passive means: parts 1 and 2. In *AGARD Rep. 768. Special Course on Skin-Friction Drag Reduction, March 2–6*, pp. 8-1 to 8-55.

DEAN, R. B. 1978 Reynolds number dependence of skin friction and other bulk flow variables in two-dimensional rectangular duct flow. *Trans. ASME* I: *J. Fluids Engng* **100**, 215–223.

DJENIDI, L., SQUIRE, L. C. & SAVILL, A. M. 1991 High resolution conformal mesh computations for V, U or L groove riblets in laminar and turbulent boundary layers. In *Recent Developments in Turbulence Management* (ed. K. S. Choi), p. 239. Kluwer.

DORF, R. C. 1983 *Modern Control Systems.* Addison-Wesley.

FAUCI, L. J. 1991 A grid-free method for high Reynolds number flow around an immersed elastic structure. *Armstrong Lab Rep.* AL-TR-1991-0045, May, pp. 1–21.

FAUCI, L. J. & PESKIN, C. S. 1988 A computational model of aquatic animal locomotion. *J. Comput. Phys.* **77**, 85–108.

FOGELSON, A. L. & PESKIN, C. S. 1988 A fast numerical method for solving the three-dimensional Stokes' equations in the presence of suspended particles. *J. Comput. Phys.* **79**, 50–69.

GOLDSTEIN, D., HANDLER, R. & SIROVICH, L. 1993*a* Modeling a no-slip flow boundary with an external force field. *J. Comput. Phys.* **105**, 354–366.

GOLDSTEIN, D., ADACHI, T. & IZUMI, H. 1993*b* Modeling flow between concentric vibrating cylinders with an external force field. *Proc. AIAA CFD Meeting, Orlando, FL.*

GOTTLIEB, D., HUSSAINI, M. Y. & ORSZAG, S. 1984 In *Spectral Methods for Partial Differential Equations* (ed. R. G. Voigt, D. Gottlieb, D. & M. Y. Hussaini). SIAM.

HANDLER, R. A., HENDRICKS, E. W. & LEIGHTON, R. I. 1989 Low Reynolds number calculation of turbulent channel flow: A general discussion. *NRL Memorandum Rep.* 6410, pp. 1–103.

HANDLER, R. A., LEVICH, E. & SIROVICH, L. 1993 Drag reduction in turbulent channel flow by phase randomization. *Phys. Fluids* A **5**, 686–694.

JIMENEZ, J. & MOIN, P. 1991 The minimal flow unit in near-wall turbulence. *J. Fluid Mech.* **225**, 213–240.

JOHANSEN, J. B. & SMITH, C. R. 1983 The effects of cylindrical surface modifications on turbulent boundary layers. *Rep.* FM-3, pp. 1–127. Dept. of Mechanical Engineering and Mechanics, Lehigh University, Bethlehem, PA.

JOHANSEN, J. B. & SMITH, C. R. 1986 The effects of cylindrical surface modifications on turbulent boundary layers. *AIAA J.* **24**, 1081–1087.

KENNEDY, J. F., HSU, S. T. & LIU, J. T. 1973 Turbulent flows past boundaries with small streamwise fins. *J. Hydraul. Div. ASCE* **99** (HY4), 605–616.

KHAN, M. M. S. 1986 A numerical investigation of the drag reduction by riblet surfaces. *AIAA Paper* 86-1127.

KIM, J., MOIN, P. & MOSER, R. 1987 Turbulence statistics in fully developed channel flow at low Reynolds number. *J. Fluid Mech.* **177**, 133–166.

KRAMER, M. 1937 Einrichtung zur Verminderurg des Reibungswide stands (Device for reducing the frictional resistance). German Patent no. 669897, March 17.

LEE, M. J., KIM, J. & MOIN, P. 1990 Structure of turbulence at high shear. *J. Fluid Mech.* **216**, 561–583.

LIU, C. K., KLINE, S. J. & JOHNSTON, J. P. 1966 An experimental study of turbulent boundary layer on rough walls. *Rep.* MD-15., pp. 1–171. Thermosciences Div., Dept of Mech. Engng, Stanford University, July.

LUCHINI, P., MANZO, F. & POZZI, A. 1991 Resistance of a grooved surface to parallel and cross-flow. *J. Fluid Mech.* **228**, 87–109.

MCQUEEN, D. M. & PESKIN, C. S. 1989 A three-dimensional computational method for blood-flow in the heart. II. Contractile fibers. *J. Comput. Phys.* **82**, 289–297.

MOIN, P., KIM, J. & CHOI, H. 1989 On the active control of wall-bounded turbulent flows. *AIAA Paper* 89-0960.

ORSZAG, S. A. 1980 Spectral methods for problems in complex geometries. *J. Comput. Phys.* **37**, 70–92.

PESKIN, C. S. 1972 Flow patterns around heart valves: a numerical method. *J. Comput. Phys.* **10**, 252–271.

PESKIN, C. S. 1977 Numerical analysis of blood flow in the heart. *J. Comput. Phys.* **25**, 220–252.

PESKIN, C. S. & MCQUEEN, D. M. 1980 Modeling prosthetic heart valves for numerical analysis of blood flow in the heart. *J. Comput. Phys.* **37**, 113–132.

PESKIN, C. S. & MCQUEEN, D. M. 1989 A three-dimensional computational method for blood-flow in the heart. I. Immersed elastic fibers in a viscous incompressible fluid. *J. Comput. Phys.* **81**, 372–405.

ROBINSON, S. K. 1991 Coherent motions in the turbulent boundary layer. *Ann. Rev. Fluid Mech.* **23**, 601–639.

SAIKI, E. & BIRINGEN, S. 1995 Numerical simulation of a cylinder in uniform flow: application of a virtual boundary method. *J. Comput. Phys.* (to appear).

SALATHE, E. P. & SIROVICH, L. 1967 Boundary-value problems in compressible magnetohydrodynamics. *Phys. Fluids* **10**, 1477–1491.

SCHRAUB, F. A. & KLINE, S. J. 1965 A study of the structure of the turbulent boundary layer with and without longitudinal pressure gradients. *Rep.* MD-12. Dept. of Mech. Engng, Stanford University.

SIROVICH, L. 1967 Initial and boundary-value problems in dissipative gas dynamics. *Phys. Fluids* **10**, 24–34.

SIROVICH, L. 1968 Steady gasdynamic flows. *Phys. Fluids* **11**, 1424–1439.

SIROVICH, L., BALL, K. & HANDLER, R. A. 1991 Propagating structures in wall-bounded turbulent flows. *Theor. Comput. Fluid Dyn.* **2**, 307–317.

SMITH, C. R. & METZLER, S. P. 1983 The characteristics of low-speed streaks in the near-wall region of the turbulent boundary layer. *J. Fluid Mech.* **129**, 27–54.

SULSKY, D. & BRACKBILL, J. U. 1991 A numerical method for suspension flows. *J. Comput. Phys.* **96**, 339–368.

TU, C. & PESKIN, C. S. 1992 Stability and instability in the computation of flows with moving immersed boundaries: a comparison of three methods. *SIAM J. Sci. Statist. Comput.* **13**, 1361–1376.

TSINOBER, A. 1990 MHD flow drag reduction. In *Viscous Drag Reduction in Boundary Layers* (ed. D. Bushnell & J. Hefner). Progress in Astronautics and Aeronautics, vol. 123, p. 327. AIAA.

UNVERDI, S. O. & TRYGGVASON, G. 1992 A front-tracking method for viscous, incompressible, multi-fluid flows. *J. Comput. Phys.* **100**, 25–27.

VIECELLI, J. A. 1969 A method for including arbitrary external boundaries in the MAC incompressible fluid computing technique. *J. Comput. Phys.* **4**, 543–551.

VIECELLI, J. A. 1971 A computing method for incompressible flows bounded by moving walls. *J. Comput. Phys.* **8**, 119–143.

VUKOSLAVCEVIC, P., WALLACE J. M. & BALINT, J. L. 1992 Viscous drag reduction using streamwise-aligned riblets. *AIAA J.* **30**, 1119–1122.

WALLACE, J. M. & BALINT, J. L. 1988 Viscous drag reduction using streamwise aligned riblets: Survey and new results. In *Turbulence Management and Relaminarisation, IUTAM Symp., Bangalore, India, 1987* (ed. H. W. Liepmann & R. Narasimha), pp. 133–147. Springer.

WALSH, M. J. 1990 Riblets. In *Viscous Drag Reduction in Boundary Layers* (ed. D. Bushnell & J. Hefner). Progress in Astronautics and Aeronautics, vol. 123, pp. 203–259. AIAA.